



# HOMOLOGOUS SOLAR EVENTS ON 2011 JANUARY 27: BUILD-UP AND PROPAGATION IN A COMPLEX CORONAL ENVIRONMENT

M. PICK<sup>1</sup>, G. STENBORGB<sup>2,3</sup>, P. DÉMOULIN<sup>1</sup>, P. ZUCCA<sup>1</sup>, AND A. LECACHEUX<sup>1</sup>

<sup>1</sup> LESIA-Observatoire de Paris, CNRS, UPMC Univ. Paris 06, Univ. Paris-Diderot, 5 place Jules Janssen, F-92190, Meudon, France

<sup>2</sup> School of Physics, Astronomy, and Computational Sciences (SPACS), College of Science, George Mason University, Fairfax, VA 22030, USA

Received 2015 August 27; accepted 2016 March 4; published 2016 May 13

## ABSTRACT

In spite of the wealth of imaging observations at the extreme-ultraviolet (EUV), X-ray, and radio wavelengths, there are still relatively few cases where all of the imagery is available to study the full development of a coronal mass ejection (CME) event and its associated shock. The aim of this study is to contribute to the understanding of the role of the coronal environment in the development of CMEs and the formation of shocks, and their propagation. We have analyzed the interactions of a couple of homologous CME events with ambient coronal structures. Both events were launched in a direction far from the local vertical, and exhibited a radical change in their direction of propagation during their progression from the low corona into higher altitudes. Observations at EUV wavelengths from the Atmospheric Imaging Assembly instrument on board the *Solar Dynamic Observatory* were used to track the events in the low corona. The development of the events at higher altitudes was followed by the white-light coronagraphs on board the *Solar and Heliospheric Observatory*. Radio emissions produced during the development of the events were well recorded by the Nançay solar instruments. Thanks to their detection of accelerated electrons, the radio observations are an important complement to the EUV imaging. They allowed us to characterize the development of the associated shocks, and helped to unveil the physical processes behind the complex interactions between the CMEs and ambient medium (e.g., compression, reconnection).

**Key words:** Sun: coronal mass ejections (CMEs) – Sun: flares – Sun: radio radiation

**Supporting material:** animations

## 1. INTRODUCTION

Coronal mass ejections (CMEs) are large-scale magnetic structures which carry a large amount of plasma and magnetic field out into the corona and interplanetary medium. Today, our understanding of their connection to other forms of solar activity is widely facilitated by coordinated multi-wavelength observations from various observational vantage points. The multi-viewpoint and multi-wavelength coverage are both key factors in shedding light on the physical processes at work during their generation and subsequent propagation.

A standard picture of a CME eruption is well summarized by the model proposed by Lin & Forbes (2000). (See also the reviews of Forbes 2010 and Aulanier 2014.) In this model, the CME is built from an initially twisted flux tube (flux rope) that is located above a photospheric polarity inversion line (PIL) which becomes unstable and erupts. The magnetic field lines overlying the flux rope are then stretched by the eruption and a current sheet (CS) is formed between the inversion line and the bottom of the erupting flux rope. Magnetic reconnection occurs along the CS, first at low altitudes and then at progressively higher ones (Forbes et al. 2006). The model also predicts the formation of post-eruptive loops behind the CS (Aulanier et al. 2012). Using numerical simulations, Janvier et al. (2015) extended this model to three dimensions and successfully compared it to photospheric and coronal observations. The first unambiguous evidence in white-light observations of the formation of a CS in the wake of a CME was reported by Lin et al. (2005; see also Vršnak et al. 2009). The various observational signatures of magnetic reconnection predicted by the model have also been observed at extreme-ultraviolet (EUV) wavelengths (e.g., Liu et al. 2010).

Before the advent of the *STEREO* mission (Kaiser et al. 2008), early studies of the CME initiation mechanisms and their early development in the low corona were primarily based on EUV observations from a single viewpoint. These early observations also suffered from a limited temporal cadence and/or relatively small field of view (e.g., Sterling & Moore 2004; Sterling et al. 2007). In recent years, the most fascinating results have arisen from the combined use of the EUV imagers (EUVI, Wuelser et al. 2004), one of the five instruments of the SECCHI telescope package on board *STEREO*, and the Atmospheric Imaging Assembly (AIA, Lemen et al. 2012) instrument on board the *Solar Dynamics Observatory* (*SDO*). By taking advantage of both the high temporal and spatial resolution, and the almost co-temporal, multi-temperature observations provided by the *SDO/AIA* instrument, Patsourakos et al. (2010) showed that CME formation begins with a slow, self-similar expansion of slowly rising loops, followed by a fast and short-lived ( $\sim 70$  s) period of strong lateral over-expansion, which essentially creates a bubble-shaped structure, namely, the CME. Afterward, the CME undergoes another phase of self-similar expansion until (at least) exiting the *SDO/AIA* field of view. The measurements showed that the EUV bubble forms when both the flare heating and CME acceleration are at their maximum levels, a fact that would indicate that magnetic reconnection may play a crucial role at this stage.

The role played by magnetic reconnection was pointed out by Cheng et al. (2011) using *SDO/AIA* multi-temperature observations. Thereafter, Cheng et al. (2013) showed that the pre-eruption structure appears as a twisted structure in the hot channels, lying along the magnetic structure of a cold filament. As reconnection develops during this impulsive phase, this structure starts to rise rapidly in the corona, forming a growing flux rope with an

<sup>3</sup> Current affiliation: Space Science Division, US Naval Research Laboratory.

observable leading front. All of these observations are consistent with the flux-rope model (e.g., Lin et al. 2004; Aulanier et al. 2010), in which magnetic reconnection induced in the CS converts the stretched surrounding magnetic field in the new poloidal flux of the flux rope. New observational evidence of this three-dimensional (3D) reconnection includes the photospheric evolution of the electric currents (Janvier et al. 2014) and the predicted slippage of the field lines (Janvier et al. 2013; Dudík et al. 2014). Furthermore, based on both 3D magnetohydrodynamic simulations and data from *STEREO*/SECCHI, Vourlidas et al. (2012) found that at least 40% of the observed CMEs exhibit clear signatures of a flux-rope structure.

Spectral and imaging radio observations have also significantly contributed to our knowledge of CMEs. They allow us to probe the solar atmosphere over a large range of altitudes with an extremely high time cadence. For example, Kliem et al. (2000) observed a long series of quasi-periodic pulsations deeply modulating the continuum in the [1–2] GHz range, slowly drifting toward lower frequencies. They proposed a model in which the pulsations of the radio flux were caused by quasi-periodic episodes of electron acceleration by magnetic reconnection in a large-scale CS (see also Karlický & Bárta 2011). The formation and development of a reconnecting CS behind an erupting flux rope was later imaged by the Nançay Radioheliograph (NRH; see, e.g., Pick et al. 2005; Huang et al. 2011; Démoulin et al. 2012).

CMEs are frequently associated with type II radio bursts, which are still the best indicators of shock formation and propagation in the corona and interplanetary medium. Coronal shocks may be generated by two different mechanisms: either as blast waves initiated by the flare pressure impulse or as piston-driven shocks. However, because of the lack of imaging observations in the majority of the cases studied, the regions where the radio emission originates, as well as the local physical conditions, cannot be properly determined. This implies that the two mechanisms mentioned are difficult to discriminate (Nindos et al. 2011). The following examples illustrate the diversity of conditions that may lead to the generation of coronal shocks. Magdalenić et al. (2010) exhibited four coronal type II bursts that were clearly synchronized with flares. In another case, the source of a type II burst was found above an X-ray rising loop associated with a CME at higher altitude (Dauphin et al. 2006). In other cases, the sources of the coronal type II bursts were found to be located near the leading edges of CMEs (Ramesh et al. 2012) or on their flanks, sometimes at significant distances from the CME front (e.g., Démoulin et al. 2012). Coronal type II bursts were also often observed conjointly with the occurrence of EUV waves (Zhukov 2011; Patsourakos & Vourlidas 2012). Furthermore, the importance of CME–streamer interactions in both the solar corona and the interplanetary medium (e.g., Reiner et al. 2003; Cho et al. 2008, 2011; Feng et al. 2012; Kong et al. 2012), or of CME–CME interactions (e.g., Gopalswamy et al. 2001; Martínez Oliveros et al. 2012; Liu et al. 2014) for the production of type II bursts, has also been emphasized. From this brief introduction, we can conclude that the study of the initiation and development of CMEs and associated shocks has been possible only in a very limited number of cases. A recent study by Zucca et al. (2014b), in which the radio spectra of a particular coronal event could be obtained simultaneously with radio, EUV, and white-light images, revealed that the CME launch and early development can differ from standard models predicting a nearly radial direction of evolution. This study also revealed the importance of

the influence of the ambient medium on both the CME development and consequent production of type II bursts.

A fraction of coronal events are significantly deflected in the corona. The first evidence of CME deflection was observed during filament eruptions, and since then their study has been (and still is) an active area of research (e.g., Panasenco et al. 2011; Bi et al. 2014 and references therein). CME deflection has been observed to be influenced, in particular, by the presence of coronal holes (e.g., Gui et al. 2011; Shen et al. 2011), and appears to be related in strength and direction to the gradient of the magnetic energy density of the extrapolated full-Sun potential field. It has been found that another cause of deflection is the amount of magnetic reconnection induced between the CME field and its surrounding features. 3D numerical simulations of observed cases have been successfully conducted (Lugaz et al. 2011; Zuccarello et al. 2012). In brief, all of the interactions leading to the deflection of a coronal event have a direct impact on the accurate prediction of its impact with a planet or a spacecraft. Therefore, their understanding is crucial in order to link remote solar observations with in situ ones, and hence to facilitate space weather forecasting (e.g., Mäkelä et al. 2013; Möstl et al. 2015).

To contribute to the understanding of the effects of the environment in the development of CMEs, and the formation of shocks and their propagation, in this paper we present a multi-wavelength study of a pair of homologous CME events that occurred on 2011 January 27. Some aspects of these two events (in particular, the identification and propagation of associated EUV waves) have already been studied (Dai et al. 2012; Kienreich et al. 2013). We complement these works with the study of the interaction between the CMEs and the ambient coronal structures as they develop in the low corona. In particular, we seek to understand the differences between the radio features observed during the development of the otherwise rather qualitatively similar CMEs, and to explain the radically different directions of propagation observed on the *SOHO*/LASCO-C2 images (Brueckner et al. 1995) with respect to the direction observed during their early development in the *SDO*/AIA field of view (i.e., westward and south–westward, respectively).

The paper is organized as follows. Section 2 provides an overview of the two homologous events (hereafter events I and II, respectively), and a description of the ambient coronal environment and its estimated magnetic field topology. After a brief presentation of event I (Section 3), we concentrate on the analysis of event II (Section 4), which is the better-documented event and less prone to radio-related ionospheric effects. In Section 5, we analyze the type II bursts observed to shed light on (i) the origin and propagation of the shocks responsible for their production and (ii) the characteristics of the coronal environment through which they propagate. In Section 6, we compile a comparative summary of both events, and discuss the role of the ambient medium in their development along with the physical implications of our analysis. Finally, we conclude in Section 7.

## 2. SOLAR ACTIVITY ON 2011 JANUARY 27

### 2.1. Multi-wavelength Observations

We used EUV data from the *SDO*/AIA instrument and from the 195 Å channel of the SECCHI/EUVI imager on board *STEREO*-A, which on the day of the event was located at 86°.5 heliographic longitude. Its vantage location allowed it to record the Sun’s activity from a quasi-perpendicular perspective to *SDO*. White-light observations from the *SOHO*/LASCO-C2 instrument

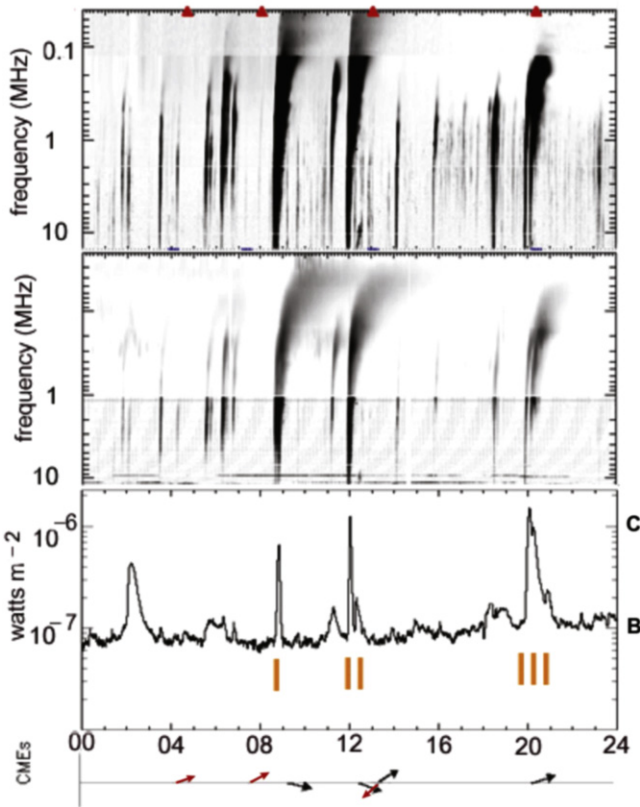


**Figure 1.** Overview of the radio and X-ray activity on 2011 January 27. Upper and middle panels: spectral radio emission measured by *STEREO-A*/SWAVES and *WIND*/WAVES, respectively. Bottom panel: time profile of the X-ray flux measured by *GOES* in the 1–8 Å range; the flare scale is indicated on the right-hand side. The labels I, II, and III point to the three main events. The direction of propagation of the associated CMEs in the *SOHO*/LASCO coronagraphs are indicated by arrows at the time of their first appearance in the *SOHO*/LASCO-C2 field of view. The arrows in red indicate that the CMEs were observed only by *SOHO*/LASCO-C2. The red triangles on the top of the figure indicate that the CMEs were also observed by *STEREO-A*.

were used to study the evolution at higher altitudes. The EUV and white-light observations were complemented by (i) radio images from the NRH (Kerdraon & Delouis 1997) in the 432–150 MHz frequency range, (ii) radio spectral data obtained with the Nançay Decameter Array (DAM, Lecacheux 2000) in the 80–10 MHz frequency range, and (iii) *WIND*/WAVES (Bougeret et al. 1995) and *STEREO*/SWAVES (Bougeret et al. 2008) radio observations in the 16–0.03 MHz frequency range.

## 2.2. A Brief Overview

Several eruptive events associated with NOAA active region (AR) 11149 were observed on 2011 January 27. These events are summarized in Figure 1<sup>4</sup> which displays an overview of the spectral radio emissions recorded by the SWAVES and WAVES instruments on board the *STEREO-A* and *WIND* spacecraft, respectively (two upper panels), and the time profile of the X-ray flux as measured by *GOES* in the 1–8 Å range (lower panel). Also, both the time of first appearance and the direction of propagation in the *SOHO*/LASCO-C2 field of view of the associated CME event are reported at the bottom of the figure (the latter with an arrow). The arrows in red indicate that the corresponding CMEs were observed only by *SOHO*/LASCO-C2, and the arrows in black point out those observed by both *SOHO*/LASCO-C2 and -C3.

**Table 1**  
List of Available Movies

Event	Movie	Time	Number
<i>SOHO</i> /LASCO-C2 white light	Run-Diff	00:00–24:00 UT	1
<i>SDO</i> /AIA 171 Å	Run-Diff.	00:12–14:12 UT	2
<i>SDO</i> /AIA 193–171 Å	Base-Diff.	11:58–12:10 UT	3
<i>STEREO-A</i> /EUVI 195 Å	Run-Diff.	00:10–23:55 UT	4

The triangles at the top of Figure 1 mark those CMEs which were also observed by COR1 on board *STEREO-A*.

The X-ray flux exhibits four main peaks. The first peak (i.e., the weaker one) is associated with faint type III bursts that have a low-frequency cut-off around 0.1 MHz and with a CME that vanishes in the *SOHO*/LASCO-C2 field of view. The other three peaks are associated with stronger interplanetary type III bursts and CME events that reach the *SOHO*/LASCO-C3 field of view (hereafter events I, II, and III as labeled in the figure). These are the three events studied by Kienreich et al. (2013).

Events I and II (the subject of this paper), unlike event III, originate in the same portion of the AR (i.e., in its southernmost part) and are associated with the eruption of a filament. The orientation of the filament before eruption is consistent with the orientation of the PIL of the AR. These are homologous events, i.e., they follow a similar trajectory and exhibit common morphological and kinematical characteristics throughout their evolution in the *SDO*/AIA and *SOHO*/LASCO-C2 fields of view, as well as in the *STEREO-A*/EUVI images. The overall evolution of events I and II is summarized in the set of movies indicated in Table 1, available as supplementary material.

A noise storm was detected on 2011 January 27 by the NRH in its whole frequency range, i.e., [432–150] MHz.<sup>5</sup> This noise storm has been taken into account to estimate the effects of the Earth’s ionosphere on the accuracy of the location of the radio sources. Indeed, the presence of the Earth’s ionosphere may lead to a systematic bias in the determination of their locations, which is attributed to variable ionospheric refraction on large-scale electron density inhomogeneities with periods of several minutes. As the angular deviation caused by these effects decreases with the inverse of the frequency square (Wild et al. 1959), the locations of the radio sources must be corrected at each frequency (Bougeret 1981). It is worth mentioning that, given the frequency dependence, the location of the radio sources is best determined at the highest frequency. In addition, more or less organized time fluctuations of the measured positions could also be observed depending on the level of ionospheric turbulence.

In order to estimate the first effect, we used the hourly expanded plots at the time of event II at both 432 MHz and 150 MHz. These plots (not shown here) show no periodic fluctuations at any NRH frequency for either the N–S or E–W directions. Therefore, we can argue that the effects of the Earth’s ionosphere on the accuracy of the location of the radio sources associated with the second event are very small, if there are any at all. Regarding the second effect, we checked the steadiness of the measured positions. By the time of the second event (i.e., near meridian transit), the half-power beam size of the NRH was 3°.7 (N–S) and 2°.3 (E–W) at 150 MHz, and 1°.3 (N–S) and 0°.8 (E–W) at 432 MHz. In absence of ionospheric

<sup>4</sup> Adapted from <http://secchirh.obspm.fr>

<sup>5</sup> <http://secchirh.obspm.fr/>

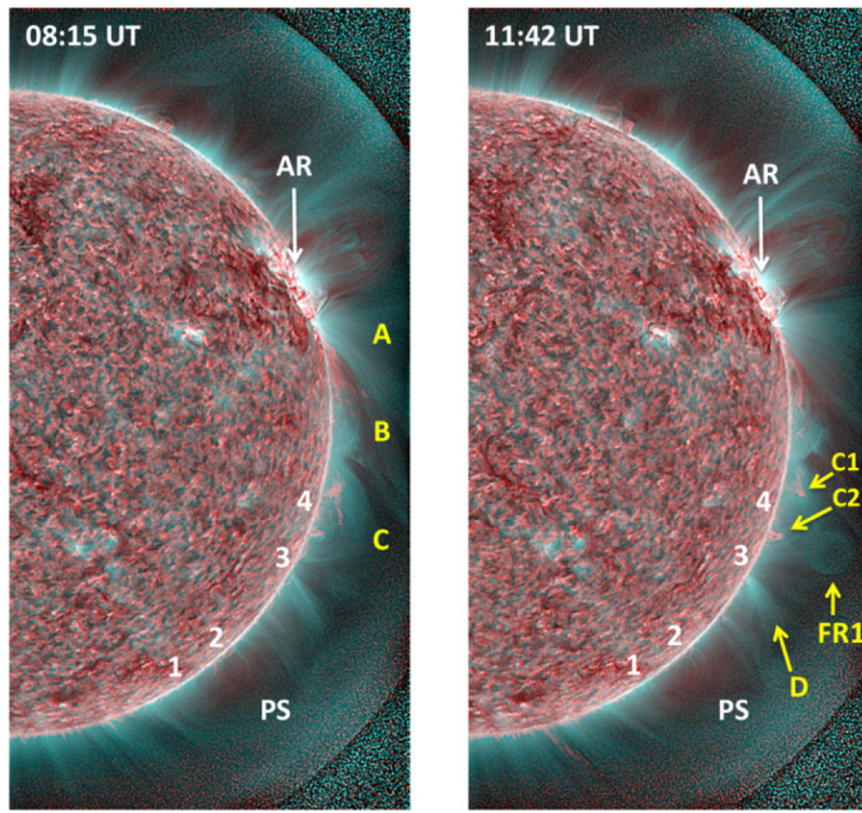


**Figure 2.** *SDO/AIA* composite images at 171 Å (blueish color) and 304 Å (reddish color) on 2011 January 27 showing the coronal configuration prior to the launch of event I (left panel) and event II (right panel), respectively. The time lag between corresponding pairs in each panel is 8 s. The source region of the events is the southern part of the AR labeled as AR. The labeled features are of interest for the events' evolution (see Section 2.3).

effects, the accuracy of the source location is estimated to be one-tenth of these values.

On the other hand, since the observations started shortly before the onset of event I, it is more difficult to estimate the impact of ionospheric effects for this event. However, as was the case later in the day, no periodic variations are detected in the corresponding hourly plots of the noise storm (not shown here). Therefore, the ionospheric effects are most likely rather small, and hence are not significant for the purposes of the present study. By 9:00 UT, the half-power beam size of the NRH was  $\sim 8.6'$  (N–S) and  $\sim 4.1'$  (E–W) at 150 MHz, and  $\sim 3'$  (N–S) and  $\sim 1.4'$  (E–W) at 432 MHz, with the accuracy of the source location being, in the absence of ionospheric effects, one-tenth of these values.

Moreover, the ionospheric conditions at decametric wavelengths also appeared to be quiet by the time of the two events (the characteristic broadband time-frequency patterns representative of a disturbed ionosphere are clearly absent on this day; Lecacheux et al. 1981; Meyer-Vernet et al. 1981).

### 2.3. The Coronal and Magnetic Field Configuration

The evolution of events I and II in the low solar corona is strongly influenced by the ambient coronal environment. To facilitate their description and analysis, in Figure 2 we show the coronal configuration prior to the occurrence of either event as observed in the 171 and 304 Å *SDO/AIA* channels. The composite frame in the left panel shows the coronal environment prior to the development of event I. In particular, in the 171 Å channel we distinguish the following: (i) a system of fine rays (labeled A) fanning out from the southern tip of the AR,

(ii) a small arcade-like feature (B), (iii) another arcade (C) overlying two small prominences in the 304 Å channel (labeled as C1 and C2 in the right panel), and (iv) a large pseudo-streamer (PS).

Likewise, the right panel of Figure 2 shows another 171 Å/304 Å composite outlying from the coronal configuration just prior to event II. In addition to the coronal structures mentioned above, at this time we note in the 171 Å channel a well-defined, relatively narrow, fan-like feature (D) and a flux-rope like structure (FR1). FR1 becomes gradually visible in this channel starting at around 11:10 UT, i.e., significantly before the occurrence of event II (see Movie 2). However, this is not seen in the *SDO/AIA* hotter channels. It appears above the structure labeled C2, partly superposed in the line of sight with the arcade labeled C. FR1 exhibits a slow rise and is already well developed by the starting time of event II. After 11:50 UT, its lateral size is observed to grow at a rate of about  $45 \text{ km s}^{-1}$ . As seen in *SDO/AIA* images at 171 Å, FR1 is well observed up to past 12:30 UT (its upper edge is already out of the *SDO/AIA* field of view by 12:04 UT). Later, the gradual decrease of contrast resulting from the superposition in line of sight with the erupting features makes it difficult to follow clearly its evolution.

To help understand the role of magnetic structures in the development of events I and II, in Figure 3 we display the coronal magnetic field configuration derived from a potential field source surface (PFSS) extrapolation (see Wang & Sheeley 1992) to the NSO photospheric field map for Carrington rotation 2106. It shows the view from *STEREO-A*. The numbers 1 through 4 point out the locations of four PILs, which are of interest for

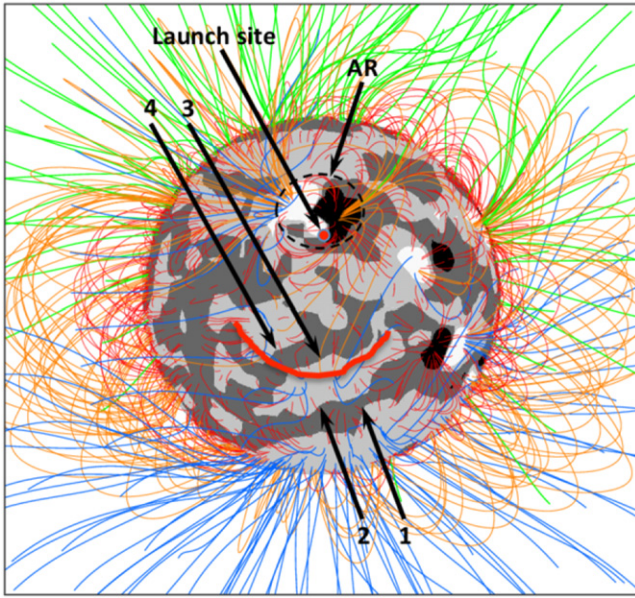


**Figure 3.** Photospheric magnetic field measured by NSO and its potential extrapolation as viewed from *STEREO-A* (Carrington rotation 2106). The dark/light gray areas depict the negative/positive radial magnetic field components. The green/blue lines represent open field lines with negative/positive photospheric polarities. The red/orange lines denote small/large closed field lines. The thick red curve marks the average extent in latitude reached by the CME bright fronts associated with events I and II as observed in *STEREO/EUVI-A* at 195 Å (see Figure 5). The numbers 1, 2, 3, and 4 indicate four polarity inversion lines (PILs).

elucidating the role of the ambient medium (their approximate location is also marked with the respective numbers in both panels of Figure 2). The red line indicates one important milestone in the development of both events: the average latitudinal extent where the two homologous events apparently stop their lateral expansion (as observed at EUV wavelengths). In the following sections, we address in more detail the description and analysis of the events' evolution.

### 3. EVENT I

Event I was associated with the short-duration B6.6 X-ray class flare SOL2011-01-27T08:50 at N10 W84 between 08:40 UT and 08:53 UT (peak at 08:50 UT).<sup>6</sup> Figures 4, 5 (upper panels), and 6 (upper panels) show a time sequence of snapshots of the event as observed in (i) the *SDO/AIA* 193 Å channel between 08:39 UT and 09:03 UT, (ii) the *STEREO-A/EUVI* 195 Å channel between 08:45 UT and 09:05 UT, and (iii) white-light images obtained with the *SOHO/LASCO-C2* coronagraph between 09:24 UT and 11:00 UT.

By around 08:33 UT, filament material is seen to flow gradually toward the southwest in the *SDO/AIA* field of view, resulting in an eruption that occurs within the time interval of the B6.6 X-ray flare. The formation of a bubble-like structure fully surrounding the filament material (structure labeled f1 in Figure 4) becomes noticeable in both the 193 and 211 Å *SDO/AIA* channels by 08:48 UT (the latter is not shown here). A bright and diffuse front is first seen by 08:50 UT in the *STEREO-A/EUVI* 195 Å images at about the same latitude (those images were taken with a time cadence of five minutes). The appearance of the bubble-like structure in the *SDO/AIA*

channels mentioned above signals the formation of a CME (hereafter CME1), although as early as 08:45 UT a very faint front could already be discerned on the limb. This bubble-like feature is seen to develop toward the southwest in the *SDO/AIA* images. Its trajectory is affected by different encounters with the surrounding coronal structures, in particular, with arcade C (see Figure 2), and it finally emerges in the *SOHO/LASCO-C2* field of view at 09:24 UT as a bright, asymmetric front developing toward the West with a linear (average) speed of  $\sim 445 \text{ km s}^{-1}$  at position angle 265°.

A series of radio type III bursts were detected by the DAM and *WIND/WAVES* between 08:37 UT and 08:50 UT (Figure 7, left panel). These type III bursts, when detected at 150 MHz by the NRH prior to 08:48 UT, originated near the southernmost edge of the eruptive bubble-like structure (represented by green triangles in Figure 4). By that time, the accuracy in the determination of the source position at 150 MHz is  $\sim 0.9$  and  $\sim 0.4$  in the N–S and E–W directions, respectively, provided that the ionospheric effects are small (i.e., about 90 pixels and 40 pixels, respectively, in a full-size *SDO/AIA* image).

The lateral expansion of CME1 can be well observed in the *SDO/AIA* 193 Å images (Figure 4; see also Movie 2). It is observed to match the development of the semi-circular front observed in *STEREO-A/EUVI* 195 Å developing in the southward direction, in both latitudinal extent and time (see Figure 5, upper panel; and also Movie 4). At first glance, the CME lateral expansion stalls at around 30° S latitude, while the front edge is deflected toward the direction finally observed in the *SOHO/LASCO-C2* field of view (see Figure 6, upper panel). Both the stall of the lateral expansion and the deflection of the main direction of propagation of the event are concomitant in time with the production of the weak and narrow-band radio bursts detected by the NRH at 150 MHz between 08:54 UT and 09:03 UT. These bursts occur near the eruptive filament, both along its southernmost edge and along the northern edge of the CME feature (their approximate location is marked with red stars in Figure 4).

Thereafter, a type II radio burst is detected by the DAM, with its onset occurring at approximately 09:03 UT (Figure 7, left panel). The type II emission profile starts fading by 09:10:30 UT and becomes indiscernible below 32 MHz after 09:15 UT. The end of the type II emission is followed by a weak type III burst detected at frequencies below 10 MHz. This type II burst exhibits only one frequency band, which can be interpreted, in principle, either as fundamental (F) or harmonic (H) emission. However, an argument in favor of the F emission interpretation is that the frequency at its onset (42 MHz) is similar to the frequency of the F emission of a second type II burst detected later in connection with event II (see Section 4.2.1 and Table 2).

After the stall of the bright front, a much fainter and diffuse EUV front is observed in *SDO/AIA* 193 Å images which continues traveling further south until a reflection of the front occurs by 09:35 UT in the vicinity of the northern edge of the southern polar coronal hole (for a complete description of the full development of the event the reader is referred to Kienreich et al. 2013). We conjecture that this diffuse front is a fast-mode magnetosonic wave which is no longer driven by the CME lateral expansion, in agreement with Kienreich et al. (2013).

<sup>6</sup> [http://www.lmsal.com/solarsoft/last\\_events\\_20110127\\_2315/index.html](http://www.lmsal.com/solarsoft/last_events_20110127_2315/index.html)

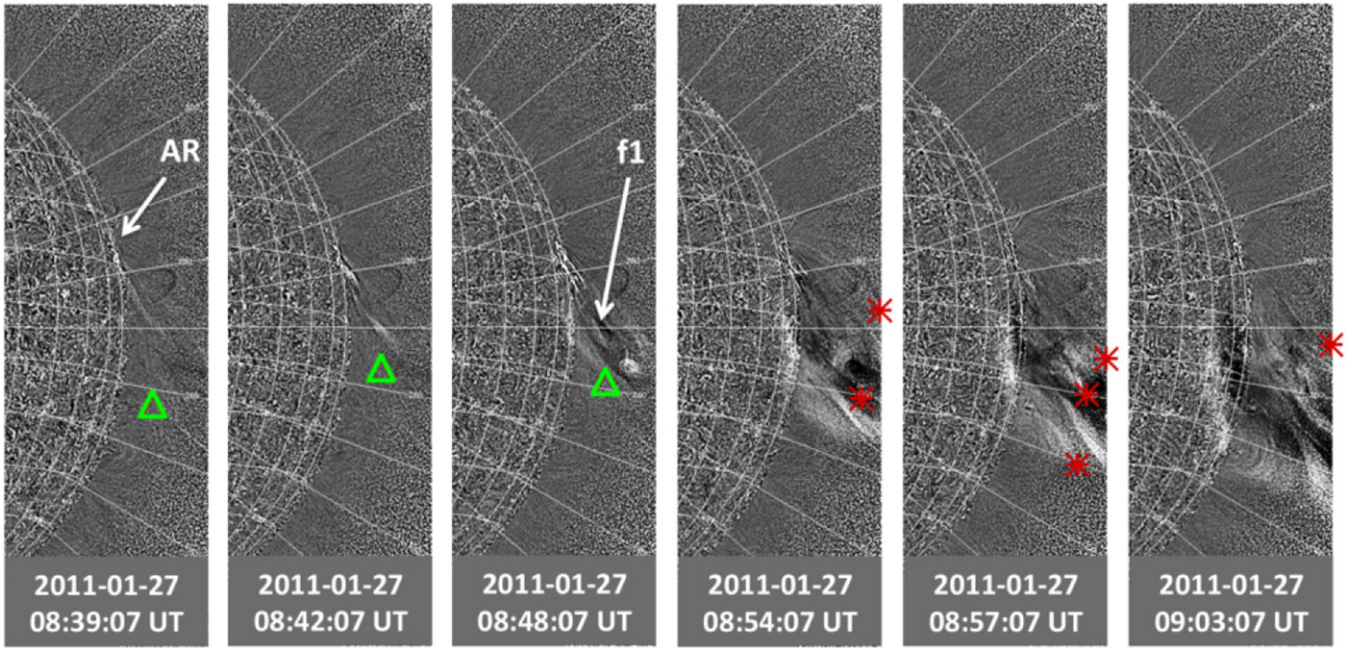


**Figure 4.** Time evolution of event I: running-difference sequence of *SDO/AIA* images at 193 Å showing the eruption of the filament f1 surrounded by a bubble-like structure. The green triangles indicate the position of the radio sources of type III/U bursts observed at 150 MHz. The red stars indicate the position of bursts detected during the encounter of the CME with arcade C (see Figure 2).

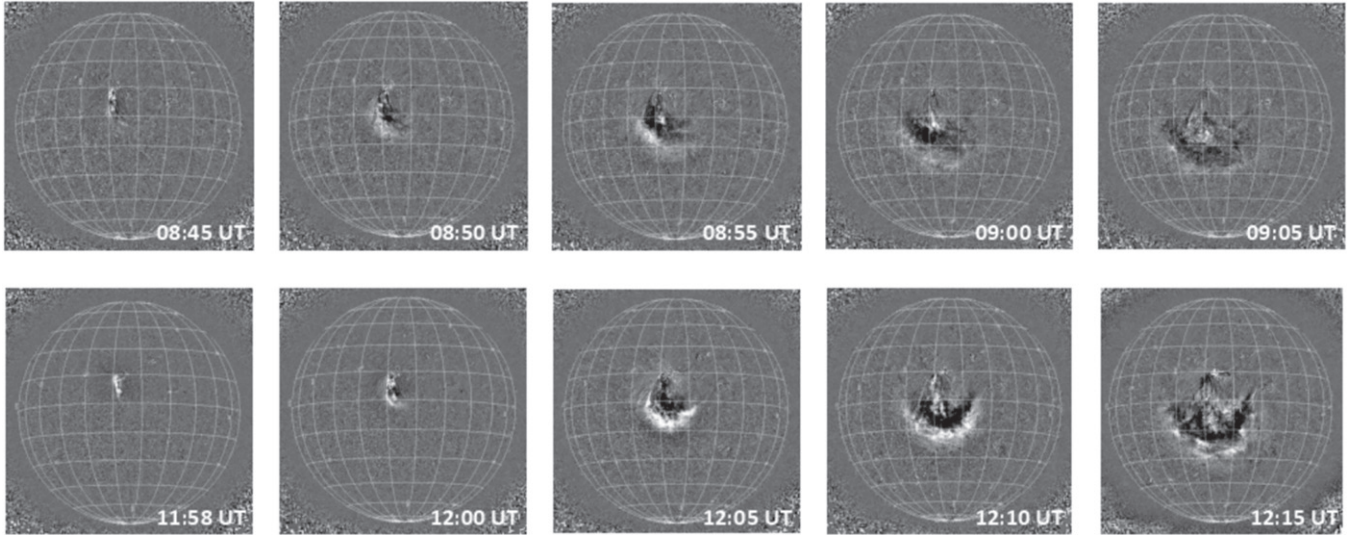


**Figure 5.** *STEREO-A* EUV running-difference images at 195 Å showing the onset and development of the EUV waves that occurred in connection with events I and II. They both apparently stop their progression at about the same latitude, i.e.,  $\sim 30^\circ$  S.  
(An animation of this figure is available.)

#### 4. EVENT II

Event II is associated with the short-duration C1.2 X-ray class flare SOL2011-01-27T12:01 that started at 11:53 UT and peaked at 12:01 UT on N12 W87,<sup>7</sup> i.e., almost at the same location as event I. Event II was preceded by a spike-like B1.6 X-ray flare that occurred between 11:05 UT and 11:22 UT, peaking at 11:16 UT on N14 W84, and followed by another

spike-like B1.9 X-ray flare on N15 W88 between 12:13 UT and 12:18 UT (see Figure 1).

As briefly mentioned at the end of Section 2.2, ionospheric effects have a small effect on the location of the radio sources observed at the time of this event. By 12:00 UT, the accuracy in the determination of the source position at 150 MHz is 0'4/0'25 for N-S/E-W, at 173 MHz is 0'34/0'20, at 228 MHz is 0'25/0'15, and at 298 MHz is 0'19/0'12. One *SDO/AIA* pixel subtends 0'6 on the Sun's surface. Therefore, by considering the largest error (i.e., 0'4), the error in the

<sup>7</sup> [http://www.lmsal.com/solarsoft/last\\_events\\_20110127\\_2315/index.html](http://www.lmsal.com/solarsoft/last_events_20110127_2315/index.html)

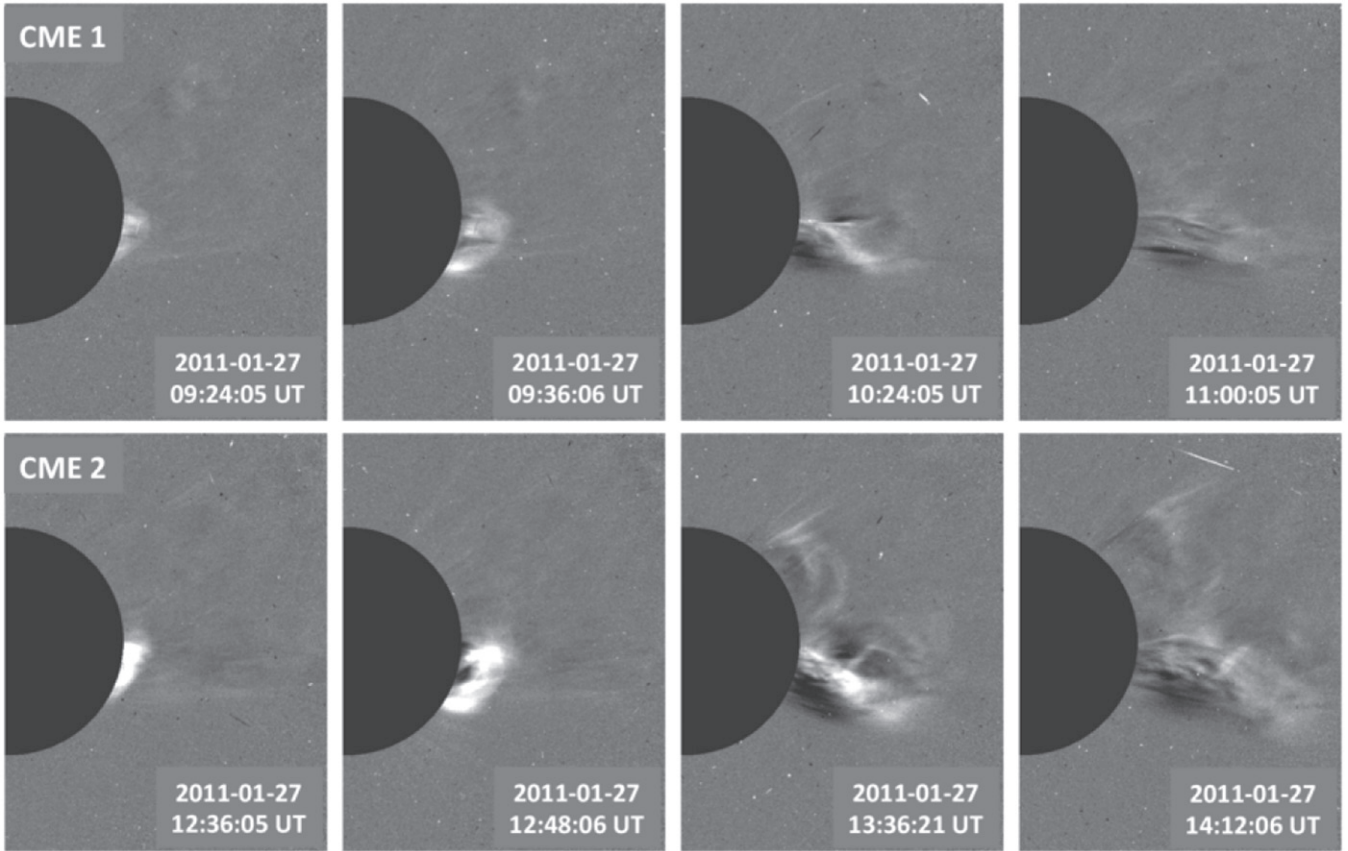


**Figure 6.** *SOHO/LASCO-C2* running-difference sequence showing the time evolution of the CMEs associated with event I (top) and event II (bottom). The running time difference for each image is 12 minutes. There was an observing gap between 12:48 UT and 13:25 UT. The panel at 13:36:21 UT shows the presence of another (faint and wide) CME located at the northern side of CME2 (time of first appearance in the *SOHO/LASCO-C2* field of view: 13:25 UT).

(An animation of this figure is available.)

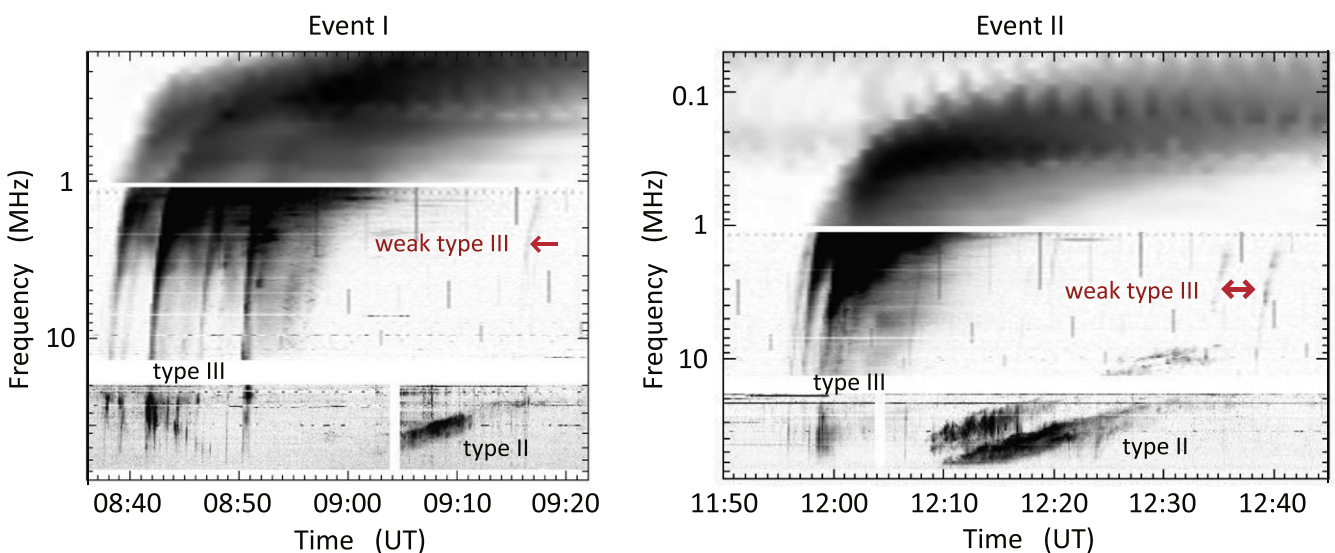


**Figure 7.** Composite radio spectra from *WIND/WAVES* and the decameter array (DAM) for events I (left) and II (right). The red arrows point out the occurrence of weak, low-frequency type III bursts.

determination of the location of the radio sources on the *SDO/AIA* images is lower than 40 pixels, which corresponds to an accuracy of about 1% for a full-size image ( $4096 \times 4096$  pixels<sup>2</sup>).

Given the more complex set of radio observations obtained during the development of event II, below we provide a comprehensive description of both its evolution and its interaction with the ambient medium.

#### 4.1. Overview

An erupting filament emerging from the southern part of AR 11149 was first detected at 11:54 UT in the different *SDO/AIA* channels developing along the same direction of the associated filament eruption as observed in event I. The filament eruption is well revealed at 304 Å (not shown here), exhibiting after 11:57 UT the signatures of a narrow, apparently twisted feature. Similar signatures appear at higher temperatures, as can be seen in the running-difference two-color composite images displayed in Figure 8 (171 Å in red, 193 Å in green; see also Movie 3). Type III emission was also observed near the onset of the event, i.e., during the time interval 11:57–12:00 UT (see Figure 7, right panel). The locations of the type III burst sources, as measured by the NRH at 150 MHz, 228 MHz, and 327 MHz, match the direction of propagation of the eruptive filament (the radio sources are marked with circles and triangles in the upper left snapshot of Figure 8).

By around 12:00 UT, the event begins to undergo a rapid evolution that is similar to that of event I. By that time, a bright, loop-like front becomes more and more visible around the filament material in the hotter *SDO/AIA* channels. These observations are consistent with the formation of a flux-rope CME (see also the running-difference image sequence in Figure 9).

As revealed in *SDO/AIA* images, the early development of the CME associated with event II (hereafter CME2) was also affected by the ambient coronal structures. In particular, CME2 began to divert upward as a result of its interaction with the arcade labeled C in Figure 2. During this time, its southern edge became increasingly brighter and more vertically oriented, resembling the development of CME1. Meanwhile, the southernmost edge of CME2 appeared to stall after 12:15 UT at around 30° S latitude. However, a diffuse and fainter front continued its way southward, becoming fainter and fainter with time (not shown here). By approximately 12:35 UT, a rather straight front began moving backward (i.e., northward), apparently from the interface between the southern edge of the PS and the northern edge of the southern coronal hole.

As seen in *STEREO-A EUVI* images obtained at 195 Å with 5 minutes cadence, bright emission starts to be observed at 11:55 UT from the southern portion of NOAA AR 11149 ( $\sim 15^\circ$  North latitude). A bright semi-circular front ahead of that bright emission is later seen developing southward by 12:00 UT, i.e., by the time the loop-like front surrounding the filament material is seen to form in *SDO/AIA* images. Several running-difference snapshots illustrating the development of the event at 195 Å are displayed in the bottom panel of Figure 5 (see also Movie 4). The large-scale intensity disturbance is characterized by a bright front preceded by a much fainter (although barely visible) diffuse front; the latter could be associated with a shock propagating ahead of the disturbance. The evolution of the bright front matches the time development of the latitudinal extent of the lateral expansion of CME2 as recorded in *SDO/AIA* images at 193 Å. It apparently stops at a latitude of roughly 30° S between 12:15 and 12:20 UT. This latitude matches the latitude reached by the off-limb counterpart of the CME (see Figure 9) around the same time. The average location where the front stalls (as seen from *STEREO-A*) is marked with a red curve in Figure 3. This figure shows that the bright front stops just after having crossed the PIL labeled 3. However, a faint and diffuse front continues

developing until it reaches the northern edge of the southern coronal hole where it is observed to be reflected. This faint and diffuse front is the signature of an EUV wave that is no longer driven by the CME. Its development matches the development of the diffuse and faint front observed in *SDO/AIA* images. We conjecture that this wave is a fast mode magnetosonic wave, in agreement with Dai et al. (2012) and Kienreich et al. (2013). The analysis of this later part of the event is beyond the scope of this paper. The reader is referred to Dai et al. (2012) and Kienreich et al. (2013) for a detailed analysis of this part of the event.

Similar to CME1, CME2 shows up in the *SOHO/LASCO-C2* field of view as a bright, asymmetric front developing westward by 12:36 UT (see Figure 6, bottom panel) with a linear (average) speed of  $\sim 485 \text{ km s}^{-1}$  at position angle 265°. The development of the event in the *SOHO/LASCO-C2* field of view will be treated in more detail in Section 4.3.

#### 4.2. The Evolution of CME2 in the Low Corona

Both the running-difference *SDO/AIA* composite images shown in Figure 8 (193 Å in green, 171 Å in red) and the snapshots in Figure 9 reveal that the leading edge of CME2 can be well discerned at 193 Å, and easily followed. The encounter between the outermost part of its front edge (seen at 193 Å) and the northern part of the pre-existing flux rope FR1 (seen only at 171 Å) occurs at  $\sim 12:06:24$  UT. The transition before and after this time is well revealed by the radio emission at several frequencies (a detailed analysis is presented in Section 4.2.1).

Figures 10 and 11 display in the right panel the time evolution of the EUV event along its principal direction of propagation as seen in *SDO/AIA* images at 171 and 193 Å, respectively. The principal direction of propagation is delineated by a continuous black line in the left panel of the corresponding figures.

At 171 Å (Figure 10, right panel), we observe a gradual change of the slope of the main bright track, i.e., a change in the speed of the brightest part of the inner core of CME2. This gradual change starts at 12:04:36 UT  $\pm 24$  s and lasts until 12:06:36 UT  $\pm 24$  s, i.e., it starts about two minutes before the encounter between FR1 and CME2. Interestingly, it occurs during the time lapse of the narrow-band radio burst activity observed to start at around 12:04 UT (denoted with red stars in Figure 12, upper panel). The rather horizontal broad white region that shows up at around 12:07 UT in the height-time map shown in Figure 10 results from the brightening of the region directly above feature C1 (see Figure 2, right panel) after the passage of the bright, inner part of CME2. By that time, a significant compression of arcade C2 (see Figure 2, right panel) is observed in both 171 and 193 Å images (arcade C2 appears partly superposed in the line of sight with FR1; see also Movie 3).

At 193 Å (Figure 11, right panel), both the track of the core of event II (hereafter FR2) and the track of the event's leading edge become visible, with the latter moving at a speed of  $620 \text{ km s}^{-1}$ . We also observe a change in the speed of FR2 which is more marked than that observed at 171 Å. This change happens at 12:04:00 UT  $\pm 24$  s, that is, near the time of the first series of narrow-band radio bursts observed in Figure 12, upper panel (red stars).

#### 4.2.1. Radio Bursts Observed During the Development of CME2 in the Low Corona

Both the kinematical analysis presented above and the NRH radio observations point out the existence of two different stages in the evolution of CME2 (i.e., before and after ~12:06 UT). The locations of the radio sources at 150 MHz during these two stages are depicted in Figure 8 (red stars and red triangles, respectively). As seen in projection on the plane of the sky, the radio sources appear to be located around FR1 and at the front edge of CME2. The first stage is characterized by weak, narrow-band radio bursts (denoted with red stars in the upper panel of Figure 12). These bursts were observed by the NRH only at 228 MHz and at 150 MHz, and thus are presumably of narrow bandwidth (except for one large type III at 12:05:30 UT). On the other hand, the second stage is characterized by the occurrence of strong type III radio bursts.

The two panels in the bottom left of Figure 12 provide a synthetic view of these two stages. Radio sources also observed by NRH at 298 and 173 MHz complete this analysis. The approximate locations of the radio sources detected before 12:06 UT are reported on the *SDO/AIA* 171 Å running-difference snapshot at 12:04 UT (we assume that the projection effects are negligible). Namely:

- i. narrow-band bursts detected at 150 MHz (red stars), and one type III burst at the front of CME2 (red triangle);
- ii. narrow-band bursts detected at three different frequencies along the interface between CME2 and FR1 (depicted by colored stars: 298 MHz in green, 228 MHz in blue, 173 MHz in yellow). The blue arrow represents the displacement of the source at 228 MHz observed between 12:06:00 UT and 12:06:25 UT (with a 1 s cadence);
- iii. weak bursts on the top of FR1 at 150 MHz and at 173 MHz (depicted by a red and a yellow star, respectively).

We also note the presence of a source detected at both 173 MHz and 150 MHz between 12:04:40 UT and 12:06:00 UT with peak intensity by [12:05:20–12:05:27] UT (depicted with a yellow and red triangle). As the corresponding emission occurs approximately at the time of the strongest burst, which is clearly identified as a type III burst by the DAM (indicated by a red triangle), the spectral identification of this source remains ambiguous. This source seems to be located near the interface between the southernmost edge of FR1 and the small adjacent coronal hole (see, e.g., Figures 2 and 3).

Likewise, the NRH radio sources detected after 12:06 UT are reported on an *SDO/AIA* 171 Å running-difference snapshot at 12:06 UT. The radio bursts are indicated with the same color code as above. The main features observed are the following.

- i. A series of strong bursts at the front of CME2, occasionally detected at three frequencies by the NRH (depicted by triangles). They are identified as type III bursts by the DAM.
- ii. Weak radio bursts in the southern portion of FR1 at 228 MHz (blue square) followed by large amplitude bursts at 173 MHz (yellow square). The time evolution of the intensity of the source at 173 MHz between 12:07:47 UT and 12:08:15 UT is plotted in the bottom right panel of the Figure 12. These bursts are both located near the location where the southernmost development of the lateral expansion of CME2 occurs.

The DAM of Nançay also detected a radio Type II burst during the development of event II, exhibiting both fundamental (F) and harmonic (H) emission bands (see Figure 7, right panel). The onset of the harmonic emission H was observed to start by ~12:08:20 UT at 84 MHz (Courtesy of C. Marqué). The onset of the F emission was observed by DAM at 12:08:30 UT, i.e., significantly later than the time at which the leading edge of CME2 starts to be visible (i.e., by around 12:01 UT at 193 Å). A detailed analysis of the type II radio bursts is presented in Section 5.

#### 4.3. The Evolution of CME2 at Higher Altitudes

The nominal cadence for the *SOHO/LASCO-C2* observations on 2011 January 27 was 12 minutes. There was, however, an observational gap after 12:48 UT until 13:25 UT. Figure 6 displays a subset of *SOHO/LASCO-C2* running-difference frames by the time of the development of CME1 and CME2 across the *SOHO/LASCO-C2* field of view (see also Movie 1). Despite the difference in brightness, the time sequence presented here allows us to notice the morphological and kinematical similarities between both events (note the time lag between consecutive snapshots). The average plane-of-sky speeds of the fastest parts of the respective CME fronts in the *SOHO/LASCO-C2* field of view (i.e., at 265° position angle) were ~445 km s<sup>-1</sup> (CME1) and ~485 km s<sup>-1</sup> (CME2). In spite of the similarities, the internal structure of CME2 appears to be more complex than that of CME1.

The more complex appearance of CME2 appears to be the result of its superposition in the line of sight with two other CMEs: (i) a wide but faint CME to the north of CME2 developing toward the northwest (first detected in *SOHO/LASCO-C2* images at 13:25 UT), and (ii) a narrow and relatively slow CME that appeared just to the south of the solar equator shortly after 11:00 UT. By 13:36 UT, the southernmost part of the faint and wide CME shows up partly superposed in the line of sight with CME2 (see Figure 6, bottom panel). This CME is likely associated with the B1.9 X-ray flare that occurred between 12:13 UT and 12:18 UT with an origin in N15 W88.

The time sequence of *SOHO/LASCO-C2* images displayed in Figure 13 shows that the narrow and relatively slow CME propagates westward, exhibiting a linear speed of ~240 km s<sup>-1</sup>. This narrow CME is overtaken by CME2 after 12:48 UT. The exact time cannot be given with precision due to the *SOHO/LASCO-C2* data gap mentioned above. As can be inferred from Figure 13, CME2 propagates partly superposed in the line of sight with this narrow CME, with both developing along the same direction. If we assume that the narrow CME propagates without experiencing any deflection and with a constant speed of 240 km s<sup>-1</sup> from a potential launch site on the limb, then its launch time would be between 09:30 UT and 09:40 UT. This time period coincides with the time at which arcade C (see Figure 2, left panel) undergoes an apparent expansion, with its southern edge becoming very bright at 171 Å (see also Movie 2). Interestingly, the apparent angular expansion of CME1 is observed to stop by around 09:30 UT at a latitude of ~30° south, i.e., close to the southern edge of arcade C. The above discussion leads us to conjecture that the narrow CME is indeed launched from a region located at about 30° south latitude, although no clear signature of a CME could be observed in the *SDO/AIA* field of view at any wavelength by that time. The lack of clear signatures at EUV wavelengths along with the expansion undergone by the arcade C points to a

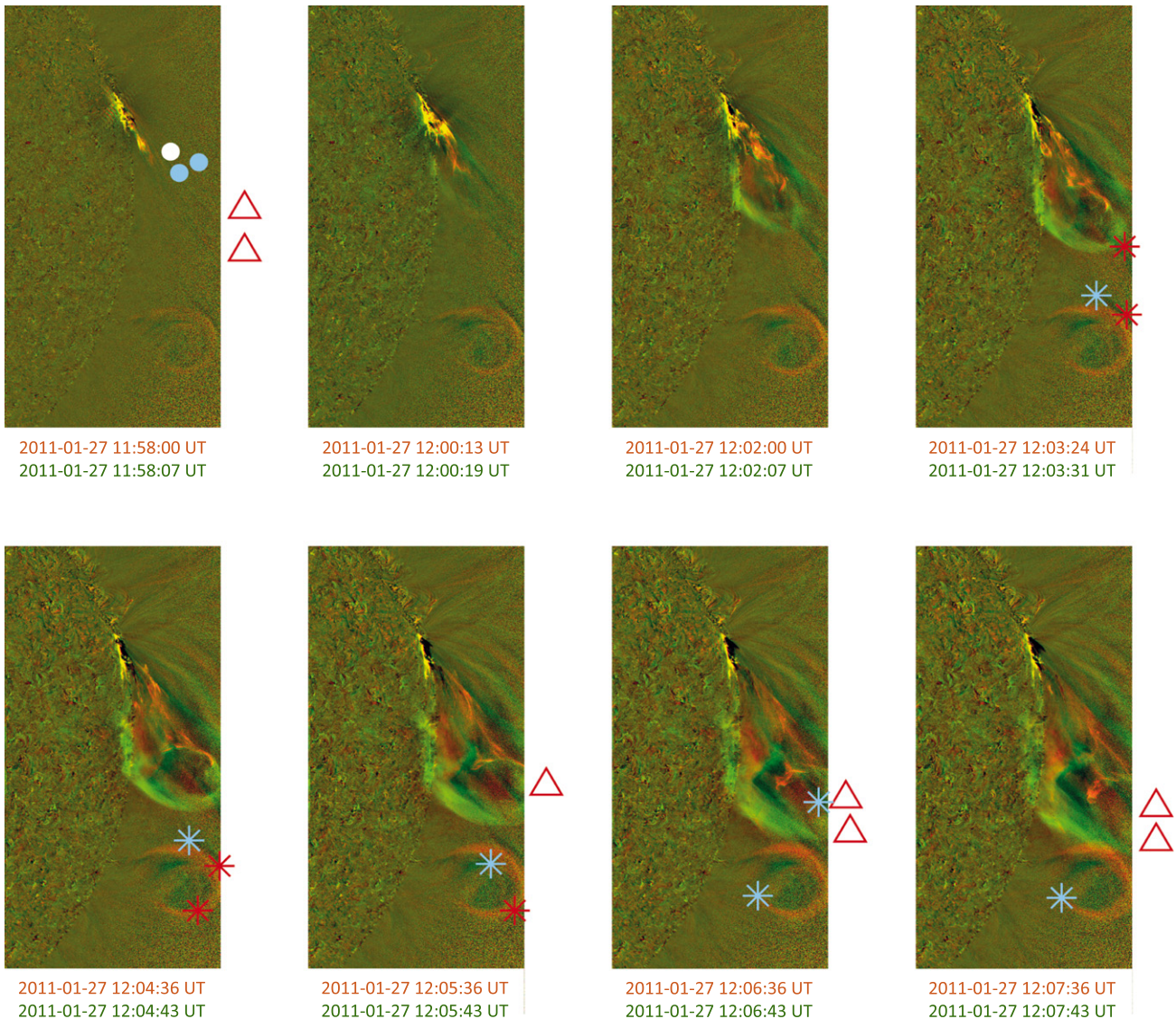


**Figure 8.** Time evolution of event II between 11:58 UT and 12:08 UT, as seen in wavelet-processed (Stenborg et al. 2008) *SDO/AIA* base-difference two-color composite images (171 Å in red, 193 Å in green, base images at 11:55:00 UT and 11:55:07 UT, respectively). Each pair has a time lag of 12 sec. The circles plotted in the first panel correspond to the location of the type III bursts observed at 228 MHz (blue color) and at 327 MHz (white color) some few minutes after the filament launch. The type III bursts observed by the NRH at 150 MHz are indicated by red triangles. The stars indicate the location of presumably narrow-band radio sources observed at 150 MHz (red color) and at 228 MHz (blue color).

(An animation of this figure is available.)

so-called “stealth CME” (see, e.g., Robbrecht et al. 2009). Further discussion on this narrow CME is beyond the scope of this paper.

## 5. ON THE PROPAGATION OF THE CME2 ASSOCIATED SHOCK

The production of type II bursts is a signature of the development of a shock wave. In the following, we describe and analyze the type II bursts observed in order to characterize the properties of (i) the shock and (ii) the ambient medium through which the shock propagates.

### 5.1. The Type II Burst: Time Evolution

An expanded view of the type II burst observed by the DAM is presented in Figure 14. The onset of fundamental type II

burst emission (F) is observed at around 12:08:30 UT. The fundamental (F) and harmonic (H) emission bands are split into two nearly parallel lanes. Following the interpretation proposed by Smerd et al. (1974), these two lanes are a consequence of the plasma emission of the upstream (fu) and downstream (fd) shock regions. To characterize the type II properties, we have identified in the figure five time segments (marked as S0 on the right panel, and S1 through S4 on the left panel) with their timing indicated in Table 2.

The first segment S0 starts by 12:08:30 UT and lasts only 30 s. During this time period, the higher-frequency lane in the F emission band is barely detected (its intensity is much weaker than the intensity of the lower frequency lane). The lower frequency lane exhibits a very narrow bandwidth, which implies that (i) the emission originates in a narrow range of plasma density and (ii) the source is well localized. The two

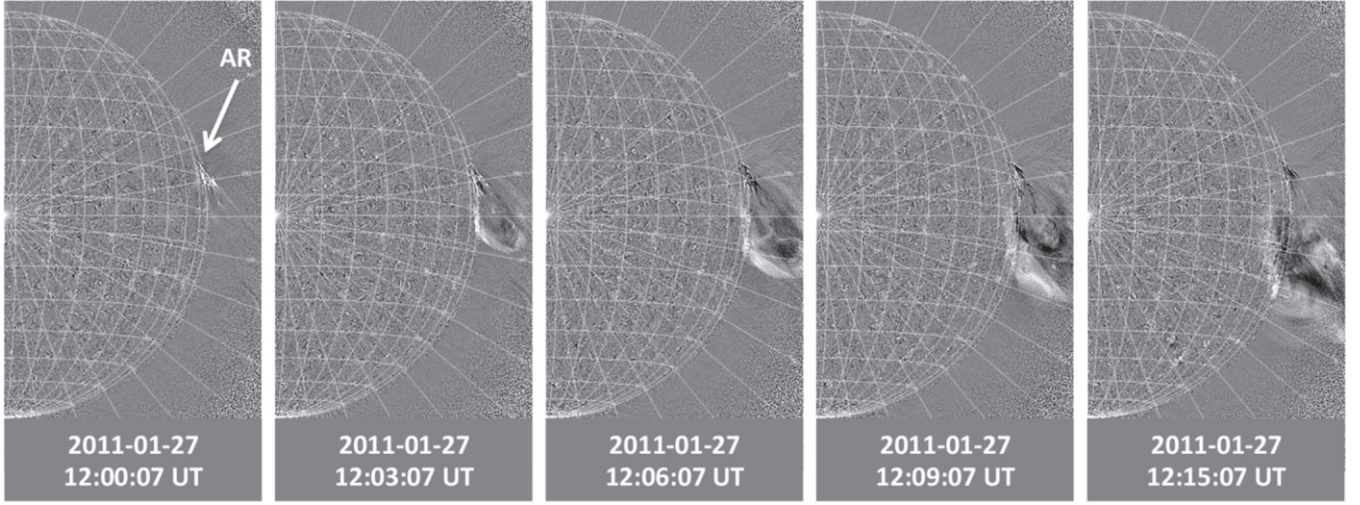


**Figure 9.** Event II. Time evolution of the CME lateral expansion, as seen in *SDO/AIA* running-difference images at 193 Å.

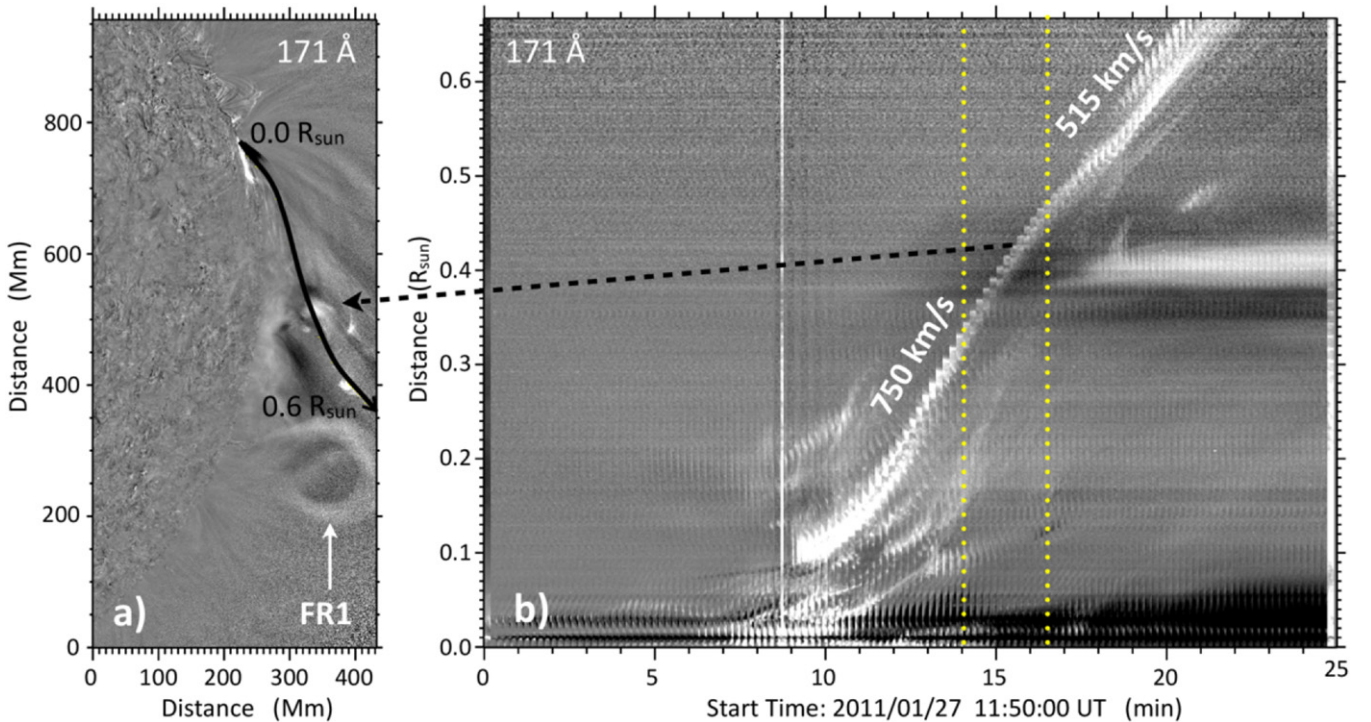


**Figure 10.** Event II. (a) *SDO/AIA* 171 Å running-difference snapshot by the time of the interaction between FR1 and CME2. The main direction of propagation followed by the core of CME2 is delineated with the continuous black line labeled with the distance along the path. (b) Time evolution of event II along the path marked with a black line in the left panel. The main bright ridge depicts the time evolution of the brightest part of the CME2 core. A progressive change in velocity occurs in the time interval [12:04:00–12:06:36] UT ± 24 s (marked with dotted yellow lines).

split lanes in the F emission band that are barely detectable during the onset of the event (segment S0) become clearly visible in segment S1. Sometime later, the H emission band also displays two split lanes (segments S2 and S3), with the lower frequency band exhibiting stronger emission.

The F emission band starts to fade at ∼12:17 UT and the H band later at ∼12:21 UT. Furthermore, after ∼12:21 UT (segment S4), a decrease of the spectral slope is discernible in the H band (it cannot be observed in the F emission due to the data gap below 21 MHz). Moreover, the two split lanes observed in the H emission band are apparently no longer

parallel after 12:21 UT, with the higher frequency lane slowly converging toward the lower frequency lane. The end of the type II burst, as observed by *WIND/WAVES* near 12:34 UT, is concomitant with the observation of weak type III bursts (Figure 7, right panel).

### 5.2. The Type II Burst: Trajectory

In the absence of radio imaging observations, assumptions need to be made to estimate the trajectory of the shock. In this work, we assumed that (i) the onset of the type II burst is

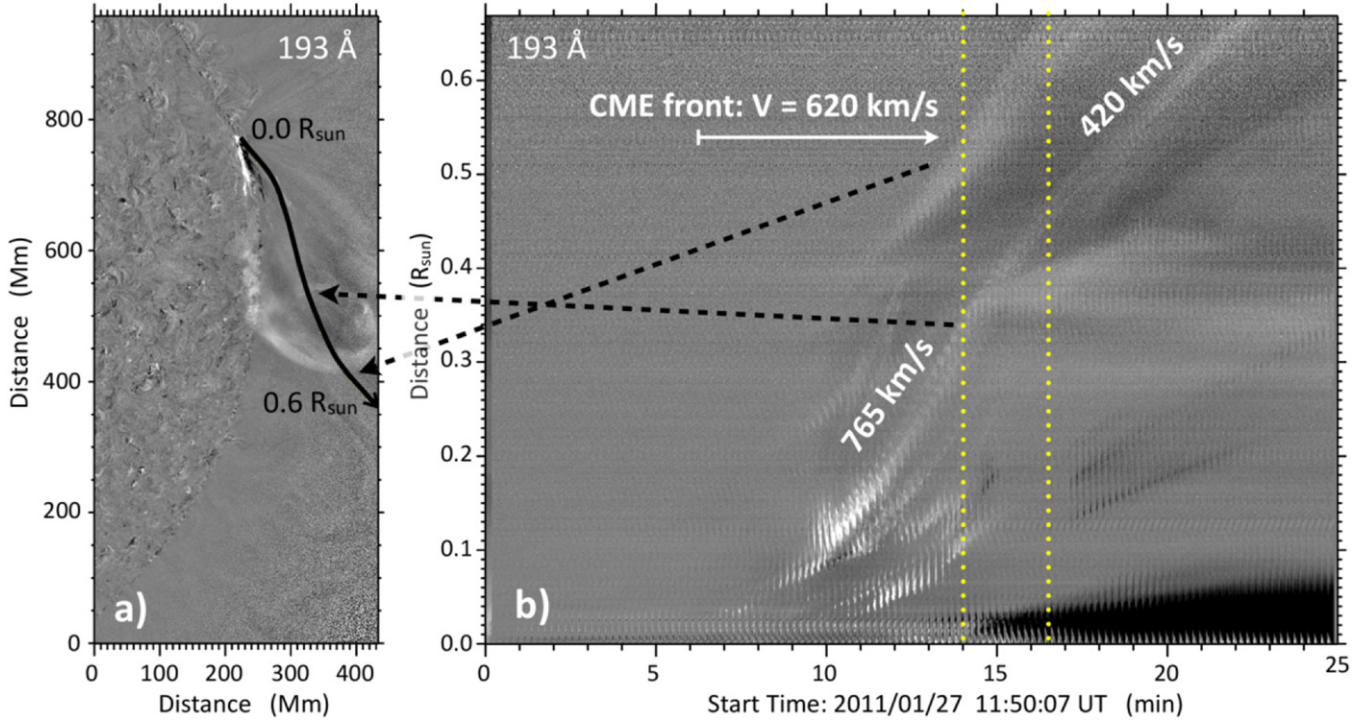


**Figure 11.** Event II. (a) *SDO/AIA* 193 Å running-difference snapshot by the time of the interaction between FR1 and CME2. The main direction of propagation followed by the core of CME2 is delineated with the continuous black line labeled with the distance along the path. (b) Time evolution of event II along the path marked with a black line in the left panel. The leading edge of the CME becomes visible at  $\sim 12:01$  UT (see the top part of the panel). The main bright ridge depicts the time evolution of the brightest part of the CME2 core. A progressive change in velocity occurs in the time interval [12:04:07–12:06:43] UT  $\pm 24$  s (marked with dotted yellow lines).

**Table 2**  
Timeline of “Type II” Radio Observations and Principal Markers Associated with Events I and II

Markers	Fundamental		Harmonic		Interplanetary Type III Bursts
	Time (UT)	Frequency (MHz)	Time (UT)	Frequency (MHz)	
<b>Event I</b>					
Onset	~09:03	42	...	...	...
Fading intensity	09:11	32	...	...	...
End	~09:12	~30	...	...	09:15
<b>Event II</b>					
Onset S0	12:08:30	42	...	...	...
End S0	12:09	39	...	...	...
Onset S1	12:09	39	...	...	...
End S1	12:10	36	...	...	...
Onset S2	...	...	12:12	54	...
End S2	...	...	12:14	47.5	...
Onset S3	...	...	12:18	37.5	...
End S3	...	...	12:21	33	...
Fading intensity	12:17	24	12:21	33	...
Onset S4	...	...	12:21	33	...
End S4	...	...	~12:28	24	...
End	~12:34	~10	~12:34	~20	12:34; 12:38

**Note.** The frequencies indicated in the table correspond to the frequencies of the downstream lanes.

associated with the CME front, and (ii) the main direction of propagation of the shock exhibits an inclination with respect to the solar equator similar to that of the CME. In particular, we tested the shock propagation along two directions:  $11^\circ$  and  $15^\circ$

toward south of the solar equator (i.e., position angles of  $259^\circ$  and  $255^\circ$ , respectively). The former corresponds to the angular location of the apex of the CME front (as seen in the 193 Å *SDO/AIA* images) by the time of the onset of the type II

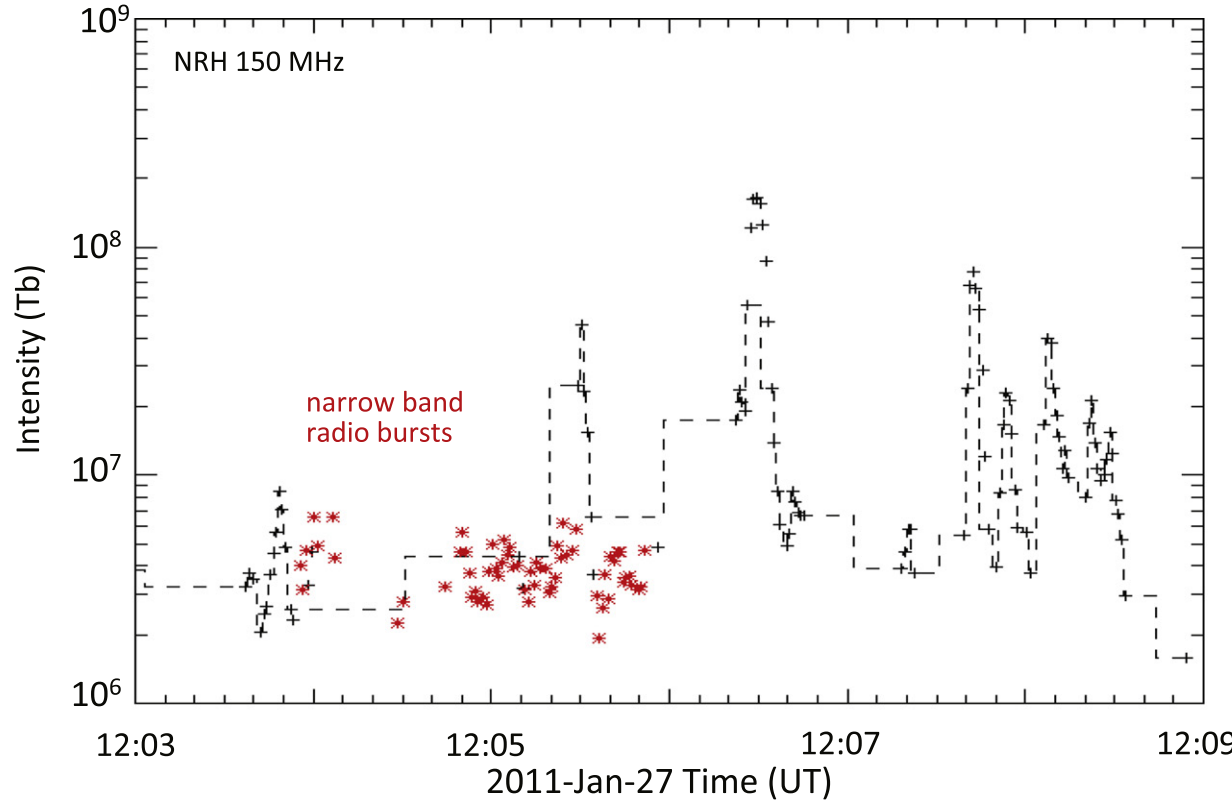


**Figure 12.** Summary of radio emissions associated with event II. The upper panel shows the time evolution of the intensity of the radio sources observed at 150 MHz after 12:03 UT (in logarithm scale). The red stars correspond to narrow-band radio bursts and the dashed lines to the type III bursts (the spatial locations of the radio sources are reported in Figure 8). The two bottom left panels show the radio sources detected by the NRH during the time intervals [12:03:30–12:06:00] UT and [12:06:00–12:08:30] UT on 171 Å running-difference snapshots at 12:04 UT and 12:06 UT, respectively. The color coding of the radio frequencies is as follows: 298 MHz: green, 228 MHz: blue, 173 MHz: yellow, and 150 MHz: red. The different symbols are used to emphasize the different kinds of emission (for details see Section 4.2.1). The right panel displays the time evolution of the flux at 173 MHz in the region indicated by a yellow square on the snapshot at 12:06 UT.

burst. The latter matches the mean direction of propagation of CME2 in the *SOHO/LASCO-C2* field of view.

The shock's speed (hereafter  $V_S$ ) can be inferred from the frequency drift of the type II burst by assuming an electron density profile that depends only on the radial distance.

Therefore, to estimate the altitude reached by the front edge of the shock, we used one and two times the Saito density model (hereafter 1-SDM and 2-SDM, respectively; Saito et al. 1977). We will justify the selection of these density models at the end of Section 5.3. We calculated the shock's altitude range in the

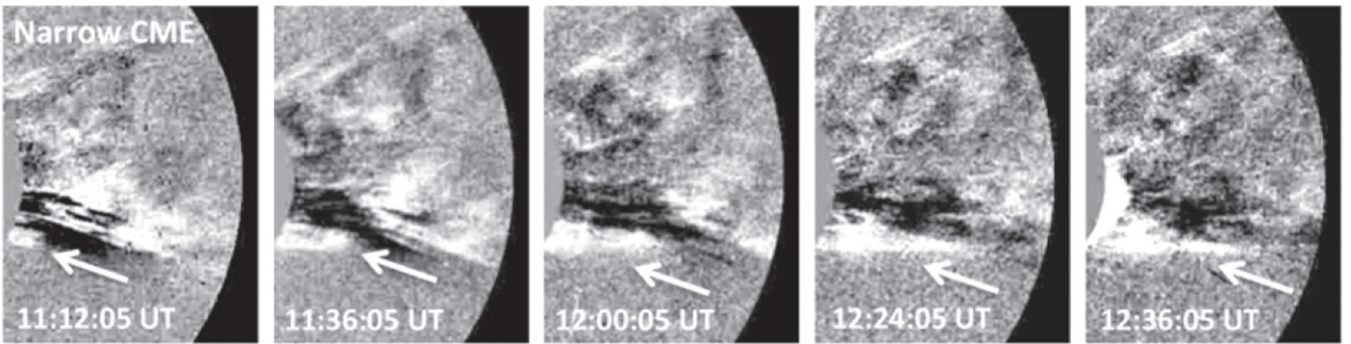


**Figure 13.** *SOHO/LASCO-C2* running-difference sequence showing the time evolution of a slow, narrow CME that develops prior to CME2 and is later overpassed. The running time difference for each image is 12 minutes. The intensity contrast has been increased to enhance the visibility of the narrow CME. For details see Section 4.3.

time interval of each segment because the frequency drift rate of the type II is not regular. For that, we use the lower frequency lanes of the F (for segments S0 and S1) and H (for segments S2, S3, and S4) emission bands at the frequencies reported in Table 2. The altitude ranges and corresponding speeds  $V_S$  of the front edge of the shock for segments 0 through 4 are displayed in Table 3 (the uncertainties in the speeds were estimated using  $3\sigma$  from the linear fit in the dynamic spectrum).

To infer the topological configuration of the solar corona at altitudes in the range of the observational gap between the *SDO/AIA* and *SOHO/LASCO-C2* fields of view, we used a potential field extrapolation of the photospheric magnetic field as measured by NSO (Figure 15). Since we are studying a west limb event, the magnetic field could have evolved during the few days present between its on-disk measurement and its value at the solar limb. Unfortunately, because of this observational gap between the fields of view of the two instruments, we cannot assess the reliability of the extrapolation by comparing it to observed structures. We can only rely on the typical slow evolution of the large-scale structures (from several days up to a few weeks for the larger scales) and the potential field approximation with the classical source surface.

Within the above limitations, we compared the estimated positions of the type II radio emission with the modeled magnetic field configuration. In Figure 15, we report the five individual segments (S0 trough S4) on two lines representing, respectively, directions along a  $15^\circ$  section for 1-SDM and  $11^\circ$  section for 2-SDM. In the dynamic spectra reported in Figure 14, a fading of the type II emission can be observed at  $\sim 12:17$  UT for the fundamental emission, and later at  $\sim 12:21$  UT for the harmonic component. The location along the CME trajectory where the fading occurs is shown in Figure 15 with green x symbols for the fundamental and green plus symbols for the harmonic. The fading of the type II F band seems to start near the transition between the magnetic arcade (delineated with the orange field lines) and the open field lines (delineated in blue color) for both 1-SDM and 2-SDM. On the other hand, the fading of the harmonic emission occurs beyond this transition region.

### 5.3. On the Shock and the Coronal Environment: the Alfvén Speed

The split in the two parallel lanes of both the F and H emission bands is a consequence of the plasma emission from before and after the shock region. This split can be used to evaluate the density jump at the shock front, which provides an estimate of the shock's Alfvén Mach number (hereafter  $M_A$ ). Vršnak et al.

(2002) developed a procedure based on this interpretation to estimate  $M_A$ . The Mach number is defined as  $M_A = V_S/V_A$ , where  $V_S$  is the shock's propagation speed and  $V_A$  is the Alfvén speed. Therefore, combined with  $V_S$ , it provides an estimate for  $V_A$ . Vršnak et al. showed that neither  $V_A$  or the magnetic field significantly depend on the choice of the plasma parameter  $\beta$  and of the propagation angle. For a low plasma parameter and a quasi-perpendicular shock, the Alfvén Mach number  $M_A$  can be written as  $M_A \sim [0.5X(X + 5)/(4 - X)]^{0.5}$ , where  $X = (f_u/f_l)^2$ , and  $f_u$  and  $f_l$  are the frequencies of the upper and lower bands, respectively. In the case of a quasi-parallel shock, the Alfvén Mach number is simply given by  $M_A = X^{0.5}$ .

The ratio  $f_u/f_l$  measured on each time segment S1, S2, S3, S4 (see Figure 14) does not vary significantly and is  $\sim 1.25$ . Assuming a quasi-perpendicular shock, we find  $M_A \sim 1.50$ , which leads to Alfvén speeds  $V_A$  along the segments S1 to S4 of  $[330 \pm 50, 290 \pm 40, 320 \pm 50, 230 \pm 20] \text{ km s}^{-1}$  and of  $[380 \pm 30, 340 \pm 40, 370 \pm 60, 280 \pm 20] \text{ km s}^{-1}$ , for densities equal to 1-SDM and 2-SDM, respectively. In the case of a quasi-parallel shock,  $M_A$  is 1.25 and the corresponding Alfvén speeds  $V_A$  for one 1-SDM and 2-SDM are  $[400 \pm 60, 350 \pm 50, 380 \pm 60, 280 \pm 30] \text{ km s}^{-1}$  and  $[450 \pm 40, 400 \pm 60, 440 \pm 80, 330 \pm 30] \text{ km s}^{-1}$ , respectively. The results are then only weakly sensitive to the relative orientation between the shock's normal and the upstream magnetic field.

Figure 16 shows the Alfvén speeds as derived from (i) the splitting of the type II burst and (ii) the method described in Zucca et al. (2014a); in both cases assuming the same two radial trajectories. The latter method combines measurements of electron density obtained from emission measures from *SDO/AIA* observations and polarized brightness from *SOHO/LASCO* data with the magnetic field strength obtained via a PFSS extrapolation of the photospheric magnetic field (for a full description of the method, the reader is referred to Zucca et al. 2014a). The two approaches provide comparable estimates of Alfvén speeds and of electron densities, where the latter is consistent with an ambient medium of low electron density. Note also that there is no significant difference between the  $V_A$  values obtained by considering inclinations of the trajectory of the type II burst at  $11^\circ$  and  $15^\circ$ .

Despite the consistency of the results for the coronal densities derived using the above methods, it can still be argued that the coronal densities derived from 1-SDM to 2-SDM are low for a region above a typical AR. In particular, this is because (i) Zucca's method uses an interpolation in the

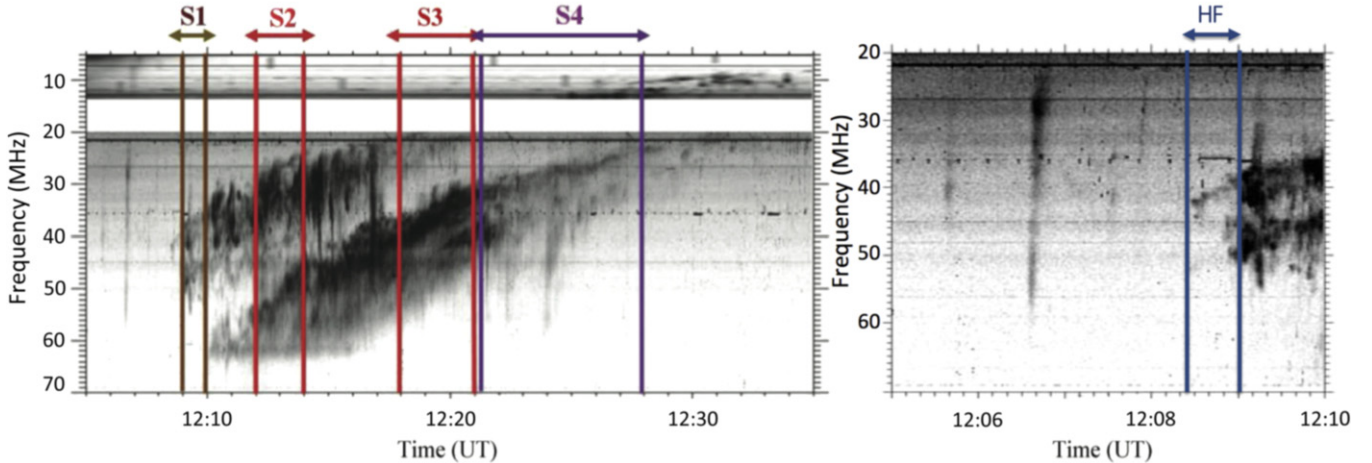


**Figure 14.** Type II burst associated with event II as observed by the DAM and *WIND/WAVES* (note the frequency gap between the highest frequency available in *WIND/WAVES* and the lowest frequency usable from the ground). The right panel shows an expanded view of the left panel in the time frame between 12:05 UT and 12:10 UT, where the onset of the event (12:08:30 UT–12:09:00 UT, segment S0) is observed to be characterized by very narrow-band emission. In the left panel, the fundamental (F) and harmonic (H) emission bands are observed to be split into two lanes. The time segments S1, S2, S3, and S4 indicate the periods for which the frequency drift and, when possible, the split between the upper and lower lanes were estimated (see Section 5).

region between the fields of view of *SDO/AIA* and *SOHO/LASCO-C2*, and (ii) our results (Figure 15) rely on a potential field magnetic extrapolation. However, this selection of densities is reasonable since (i) CME2 seems to be launched from the border of an AR, and (ii) its early trajectory appears to be highly inclined with respect to the local vertical (the ambient medium forces CME2 to propagate away from the AR above a nearly quiet Sun region; see Figures 2 and 3). Hence, the shock’s onset occurs far away from the AR.

The shock’s speed measured along segment S4 is significantly smaller than the corresponding speeds measured along the three other segments. This fact suggests that the shock develops in a different medium, which is also consistent with the change in intensity of the type II radio burst. Moreover, the resulting estimated shock’s speeds (Table 3) are comparable to the speed of the outermost part of the leading edge of CME2 as measured in the *SOHO/LASCO-C2* field of view ( $\sim 485 \text{ km s}^{-1}$ ), which further supports the choice of 1-SDM and 2-SDM for the estimation of the coronal densities. We also tried larger density values, but the results were less consistent between the different methods.

## 6. DISCUSSION

In this study, we have presented an analysis of two homologous CME events based on both multi-wavelength imaging and spectral data. The events were launched within a time interval of three hours from the same AR near the western solar limb (as seen from Earth). Both events exhibited similar, strong deflection before reaching the inner edge of the *SOHO/LASCO-C2* field of view.

To help understand the causes that led to the radical change of direction, this study focused on (i) the analysis of the early development of the events (i.e., below  $1.25 R_{\odot}$ ), paying particular attention to their interaction with the ambient coronal structures at EUV wavelengths, and (ii) the characterization of the CME-driven shock waves accompanying their development.

### 6.1. On the Early Development of the Events

The early development of events I and II presents all of the characteristics typically found in many CME events.

- i. An initiation phase characterized by a filament eruption, which rapidly evolves into a complex, elongated, twisted structure.
- ii. Production of type III radio bursts along the trajectory followed by the eruptive filament during the early stages of its evolution (we interpret the presence of the type III emission as a result of magnetic reconnection with the neighboring pseudo-open magnetic field lines).
- iii. Formation of a CME within a few minutes after the initiation phase.

However, both events exhibit two important and somehow unusual characteristics. The first is the non-radial launch of the filaments during the initiation phase, and the consequent non-radial evolution of the associated CMEs (southward of the AR rather than along the local vertical). This is due to the presence of a relatively high magnetic field region directly above the AR, which constrains the development of the event, starting on the side of the AR, away from that direction (see, e.g., Dai et al. 2012). The second unusual characteristic is the strong interaction of the CMEs with the ambient medium in the low corona. As a result of this interaction, both events underwent similar development, experiencing both a deceleration and a strong, rather abrupt change of the original direction of propagation within the same latitude range and a comparable time frame. A great part of the analysis carried out was intended to identify the coronal structures responsible for this abrupt deflection observed by both CMEs.

Despite the morphological and kinematical similarities exhibited by both events during their evolution, a topological change in the coronal configuration exists prior to the occurrence of the second event. This change is signaled by the appearance of flux rope FR1 at around  $30^{\circ}$  S latitude a couple of hours after the passage of CME1 (see, e.g., Figure 2). This new structure is only observed at 171 Å, i.e., in a particular temperature regime. Therefore, it was either a

**Table 3**  
Altitude Range and Speed of the Shock Associated with Event II

Segment	Time Range	1 × SDM		2 × SDM	
		(UT)	Altitude Range ( $R_{\odot}$ )	$V_s$ (km s $^{-1}$ )	Altitude Range ( $R_{\odot}$ )
S0(F)	12:08:30–12:09:00		...	~815	...
S1(F)	12:09–12:10		1.45–1.49	$500 \pm 80$	$1.63–1.66$
S2 (H)	12:12–12:14		1.64–1.70	$440 \pm 60$	$1.85–1.94$
S3 (H)	12:18–12:21		1.86–1.95	$480 \pm 80$	$2.06–2.21$
S4 (H)	12:21–12:28		1.95–2.10	$350 \pm 40$	$2.22–2.55$

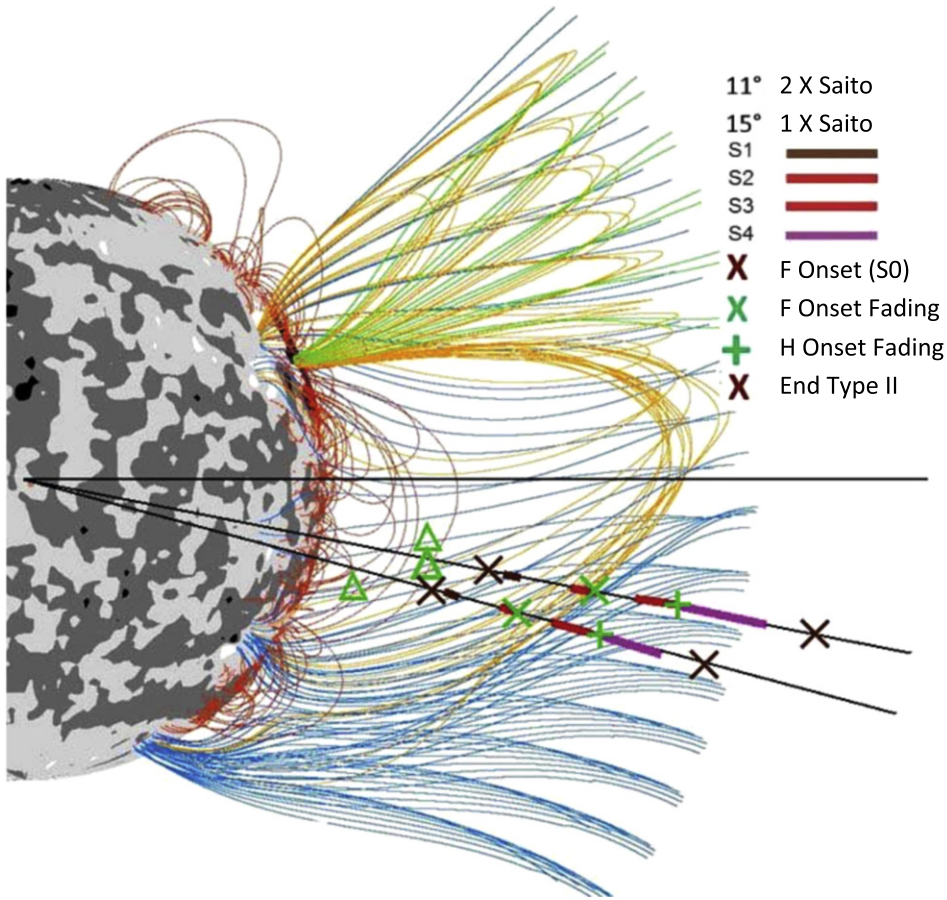


**Figure 15.** Estimate of the type II burst locations on top of a potential field extrapolation. The height of the type II burst is estimated from the spectra (Figure 14) and a coronal density model (Saito et al. 1977). The results are shown on two radial directions with inclinations of  $11^{\circ}$  and  $15^{\circ}$  and with two times and one time the density of Saito's model, respectively. The color and shape coding of the points indicate the time of the onset/end of the type II burst and of the onset of F/H intensity fading (see the insert). The color lines indicate the time intervals of the successive segments (see Figure 14 and Table 2). The green triangles indicate the positions of types III bursts observed at the EUV CME front edge after 12:05:30 UT. The photospheric magnetic field is represented with dark/light gray levels for the negative/positive radial magnetic field component. The green/blue lines are open field lines with negative/positive photospheric polarities. The red/pink/orange lines are tiny/small/large closed field lines.

pre-existent structure at a temperature outside the coverage of the *SDO/AIA* channels before the onset of event I or it simply did not exist. The richer set of radio emissions produced during the second event favors the latter. In particular, during the CME2 approach to FR1, a series of metric bursts were detected which were observed to be produced in a region between the southern edge of CME2 and FR1, as well as all around FR1 (see, e.g., Figure 8).

As seen at EUV wavelengths (in particular at 171 and 193 Å), both CME1 and CME2 are observed to gradually decrease their speeds along the principal direction of propagation. The change in speed coincides with the change of

direction, which in the case of CME2 occurs by the time the first series of radio bursts is observed (the onset of these radio bursts occurs at about two minutes before the interaction of CME2 with FR1). These observations suggest that the radio bursts observed during the approach and subsequent interaction of CME2 with FR1 are mainly the consequence of the compression exercised by the outer edge of the CME2 global structure, both on FR1 and on the region between them.

In particular, the approach of CME2 to FR1 is concomitant with the production of radio emission at different frequencies from several sources, which appeared to be aligned along the interface between the northern edge of FR1 and the southern

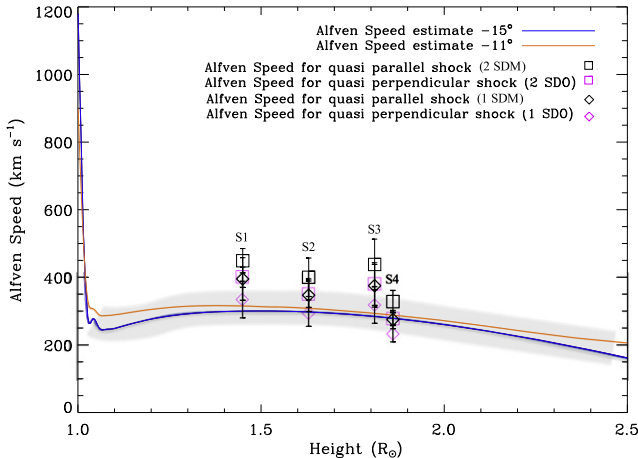


**Figure 16.** Comparison between the Alfvén speeds obtained (i) from the band splitting of the type II burst of event II (depicted by square and diamond symbols, see insert), and (ii) with the method described in Zucca et al. (2014a) for inclinations of  $11^\circ$  and  $15^\circ$  toward south of the ecliptic (depicted with orange and violet continuous lines, respectively). The gray band indicates an uncertainty of the order of 20% on the Alfvén speed estimation.

edge of CME2. This occurs at roughly the latitude of the PIL 4 (see Figure 2). Therefore, a plausible origin of these metric radio bursts is the formation of CSs at the interface region as a result of magnetic reconnection with the consequent production of accelerated particles. While CME2 continues its lateral southward expansion, FR1 sustains a steady development which slowly increases its size in all directions. The lateral pressure that both CME2 and FR1 apply to the ambient medium is well revealed by the presence of radio bursts at latitudes above the PIL 3, which are close to region D (Figures 2 and 8).

In spite of the presence of flux rope FR1, the lateral expansion of the two CMEs was observed to stall at about the same latitude (i.e.,  $\sim 30^\circ$ ) and within the same time interval in the *SDO/AIA* images taken in the EUV hotter channels (e.g., at 193 and 211 Å). Moreover, both CMEs show up later in the *SOHO/LASCO-C2* images at around the same location after a comparable time interval, propagating westward. The analysis carried out led us to conclude that the large arcade C (see Figure 2) overlying the two small prominences C1 and C2 was mainly responsible for the upward deflection of the events.

## 6.2. On the Associated Shock Waves

Both events were associated with the production of type II bursts. In particular, the first event was associated with a weak, single burst: since both its duration and its frequency range are comparable to those of the fundamental (F) emission mode of the second event (assuming that the plasma environment was similar during the two events), it presumably corresponds to the fundamental emission mode (compare the panels of Figure 7). On the other hand, the second event was associated with a stronger type II burst, exhibiting both the fundamental (F) and harmonic (H) emission modes (both modes split in two parallel lanes). Since the type II burst associated with the second event was stronger and its spectrum displayed more ample variation, we focused on the analysis of this event.

Within the two minutes preceding the onset of the second type II burst, impulsive metric radio bursts were detected, including a few type III bursts. Their sources were located

above the CME2's front edge. Part of these emissions could originate from reconnection between the erupting magnetic structures and the surrounding open coronal structures, as already observed in other events (e.g., Pick et al. 2005; Huang et al. 2011).

We also investigated the influence of the ambient medium on the evolution of the type II burst. The speed of the shock was estimated along two radial directions (i.e., at  $11^\circ$  and  $15^\circ$  toward south of the ecliptic). These directions were selected as representative of the direction of propagation of the CME during (i) the encounter with the structures responsible for its deflection and (ii) its propagation across the *SOHO/LASCO-C2* field of view, respectively. The observed drift rate of the type II was converted into the shock's speed, assuming one and two times the Saito electron density model. Based on these estimates, the shock propagated with an average speed between 480 and 560 km s<sup>-1</sup>, which is comparable to the average speed of the fastest part of CME2 in the *SOHO/LASCO-C2* field of view (485 km s<sup>-1</sup>). Then, while the downstream component of the shock (higher frequency lane) keeps moving at a similar speed, the upstream component (lower frequency lane) slows down, exhibiting an average speed between 350 and 420 km s<sup>-1</sup>. Afterward, both lanes become progressively weaker until the type II finally disappears.

We also compared the progression of the type II burst with the magnetic field configuration resulting from a potential extrapolation of the photospheric magnetic field along these directions. Within the validity of the magnetic field extrapolation, our results strongly suggest that the shock's geometry below  $\sim 2 R_\odot$  is intermediate between quasi-perpendicular and quasi-parallel (with an estimated Alfvén Mach number  $M_A$  of  $\sim 1.5$ ). Further out, after crossing a large arcade and reaching a region of open field lines, it becomes mainly quasi-parallel (with  $M_A \sim 1.25$ ). In this region, the intensity of the type II burst diminishes and vanishes shortly afterward, as expected in a quasi-parallel propagation regime.

An abrupt fading of the intensity for the F and H emission was observed. This fading indicates that the physical conditions leading to the radio emission have changed. This phenomenon is generally attributed to type II bursts entering into a region with a higher Alfvén speed profile (see, e.g., Mann et al. 1999; Vršnak et al. 2002). However, our measurements of the Alfvén speeds show no direct evidence of this in the case studied (see Figure 16). Nevertheless, we found fading near the transition from a large-scale arcade to an open magnetic field region (see Figure 15), which is in fact a transition to a lower plasma density region (higher Alfvén speed). This result is, however, limited by the absence of radio imaging observations at decameter wavelengths. Moreover, as already mentioned above, the magnetic field extrapolation has its own limitations. Still, this transition to the open field is confirmed by the occurrence of weak interplanetary type III bursts near the end of the two type II bursts (Figure 7). Similar signatures resulting from the transition between two different coronal environments has also been observed in former studies (see, e.g., Pick et al. 2005).

The fading of the H component occurred  $\sim 7$  minutes later than the fading observed in the F band. Several reasons could explain this effect; for instance, the physical conditions responsible for the conversion of plasma waves into electromagnetic waves (e.g., the distribution function of the accelerated electrons) or the properties of the medium itself.

In recent years, a large number of studies were concerned with the development of theoretical models for type II burst emission (Knock et al. 2003; Knock & Cairns 2005; Schmidt & Cairns 2012, and references therein). These models investigated the effect of the successive physical processes that produce type II burst emissions: acceleration of electrons at the shock, formation of electron beams, growth of Langmuir waves, and conversion of Langmuir energy into radiation. The predicted variations of the emissions were compared with the observations (mainly in the interplanetary medium). In particular, it was shown that the intensity of the F and H emissions of a shock propagating in an inhomogeneous solar wind are not equally sensitive to the same parameters. These theoretical results are a plausible way to interpret the observed different time evolution of the intensity fadings. However, a detailed discussion of the origin of this effect is beyond the scope of this study.

## 7. CONCLUSIONS

The goal of this work was to contribute to our understanding of the role of the coronal environment in the development of CME events, the formation of shocks, and their propagation. We chose two successive homologous events for which EUV and white-light imaging along with spectroscopic and radio imaging were available. The main findings are summarized as follows.

Both CMEs were formed in association with eruptive twisted filaments, which were launched from the same region of the Sun far from the radial direction (closer to the local horizontal). This geometry favored their interaction with the ambient medium in the low corona. The change from the original direction of propagation started, in both cases, with an encounter with a large magnetic arcade located away from the launch site. As a result, they both deflected upward, developing along a similar (almost radial) direction in white-light coronagraph images.

Both CMEs exhibited a classical impulsive phase. The second CME encountered the presence of a swiped (cleaned) environment and a flux rope (FR1), which became visible after the passage of the first CME. The interaction of the second CME with FR1 resulted in their compression/reconnection with the consequent emission of metric radio bursts, which appeared as a signature of the interaction process. The second CME showed up in the *SOHO/LASCO-C2* field of view exhibiting more complex morphology. The more complex internal structure was due to its merging, at least along the line of sight, with a slow, narrow CME on its southern part and with another faint, wide CME on its northern part.

Our analysis focused on the second event, with the objective of better understanding (i) the influence of the ambient medium during its progression, and (ii) the origin and properties of the associated shock. We summarize as follows.

1. Radio emission of short duration marked the onset of the type II burst. Furthermore, the NRH detected a series of radio bursts at the onset of the type II burst, their sources are apparently located above the CME front. Moreover, the shock's onset occurred by the time the fastest part of the CME2 front was just outside the *SDO/AIA* field of view (as seen at 193 Å). During its propagation across the *SDO/AIA* field of view, the CME front developed with a

linear speed of  $\sim 620 \text{ km s}^{-1}$ , as measured along its main direction of propagation (i.e., toward southwest). As already reported for other events (e.g., Zimovets et al. 2012; Zucca et al. 2014b), the shock's source at its onset was strongly accelerated during a short time period and moved faster than the CME leading edge (between  $815 \text{ km s}^{-1}$  and  $900 \text{ km s}^{-1}$ ). Then, the shock's speed became compatible ( $500\text{--}570 \text{ km s}^{-1}$ ) with the speed of the CME front within the error bars. This finding agrees with the conclusions from a former study (Nindos et al. 2011) regarding a CME-driven shock. In that study, Nindos et al. (2011) showed that the kinematics of the shock wave was broadly consistent with the kinematics of the associated CME, as inferred from both EUV and coronagraph observations. Based on this evidence, it is plausible to infer that the shock would have been driven by the CME.

2. The type II burst was characterized by fading intensity, which occurred at different times for the fundamental (F) and harmonic (H) emission modes. Within the assumptions made, the intensity fading was found to be associated with the progression of the shock out of a large magnetic arcade.
3. Based on the assumptions made during the analysis, we conjecture that the CME-driven shock would have interacted along its propagation with (i) an intermediate parallel/perpendicular magnetic field topology below  $\sim 2 R_\odot$ , and (ii) a quasi-parallel geometry after later encountering the open magnetic field region.
4. We derived the speed and Alfvén Mach number of the shock assuming an electronic density model. The values obtained were in agreement with those obtained using an alternative method (Zucca et al. 2014a). Moreover, the estimated speed of the shock and the average speed of CME2 (as projected into the plane of the sky) computed along its transit across the *SOHO/LASCO-C2* are consistent.

In summary, the two selected events underwent a large deflection in the low corona, crossing the ecliptic plane during their development from their source at about  $15^\circ \text{ N}$ , to finally emerge above  $\sim 2.5 R_\odot$  at an approximately symmetric location in the southern hemisphere following a radial direction of propagation which is close to the ecliptic plane. The availability of images from a combination of EUV imagers in quadrature, combined with data from white-light coronagraphs, spectral and imaging radio telescopes, and a photospheric magnetograph allowed us to unveil the processes involved in the development of the two complex events studied, and hence proved to be key ingredients to understanding how CMEs can be deflected in the low corona. The investigation revealed the key role of the local coronal environment in the development and propagation of CMEs and their associated shocks, in agreement with the results obtained in the case study presented by Zucca et al. (2014b); namely, that the ambient medium may exert a strong influence in their propagation as well as in the properties of the associated shock. Therefore, understanding the role of the coronal environment in the vicinity of the CME's source region is an important factor for establishing the link between the observations of EUV imagers and white-light coronagraphs, and hence for space weather purposes.

We thank the referee for the careful consideration of the manuscript and the helpful comments which helped improve the paper. The AIA data used here are courtesy of *SDO* (NASA) and the AIA consortium. The SECCHI data are courtesy of *STEREO* and the SECCHI consortium. The *STEREO/SECCHI* data are produced by a consortium of NRL (USA), LMSAL (USA), NASA/GSFC (USA), RAL (UK), UBHAM (UK), MPS (Germany), CSL (Belgium), IOTA (France), and IAS (France). *SOHO* is a project of international cooperation between ESA and NASA. The work of G.S. was partly funded by NASA contract NNX11AD40G and NSF award AGS-1155015. M.P. acknowledges the support from the Centre National d'Etudes Spatiales and (CNES) and from the French program on Solar Terrestrial Physics (PNST) of CNRS/INSU. The NRH and DAM are both funded by the CNRS and by the Paris Observatory. We are also grateful to Yi-Ming Wang for providing us the coronal extrapolation of the photospheric magnetic field and to Mark Linton for his helpful comments and corrections of the manuscript.

## REFERENCES

- Aulanier, G. 2014, in IAU Symp. 300, Nature of Prominences and their Role in Space Weather, ed. B. Schmieder, J.-M. Malherbe, & S. T. Wu (Cambridge: Cambridge Univ. Press), 184
- Aulanier, G., Janvier, M., & Schmieder, B. 2012, *A&A*, 543, A110
- Aulanier, G., Török, T., Démoulin, P., & DeLuca, E. E. 2010, *ApJ*, 708, 314
- Bi, Y., Jiang, Y., Yang, J., et al. 2014, *ApJ*, 790, 100
- Bougeret, J. L. 1981, *A&A*, 96, 259
- Bougeret, J. L., Goetz, K., Kaiser, M. L., et al. 2008, *SSRv*, 136, 487
- Bougeret, J.-L., Kaiser, M. L., Kellogg, P. J., et al. 1995, *SSRv*, 71, 231
- Breuckner, G. E., Howard, R. A., Koomen, M. J., et al. 1995, *SoPh*, 162, 357
- Cheng, X., Zhang, J., Ding, M. D., Liu, Y., & Poomvisees, W. 2013, *ApJ*, 763, 43
- Cheng, X., Zhang, J., Liu, Y., & Ding, M. D. 2011, *ApJL*, 732, L25
- Cho, K.-S., Bong, S.-C., Kim, Y.-H., et al. 2008, *A&A*, 491, 873
- Cho, K.-S., Bong, S.-C., Moon, Y.-J., et al. 2011, *A&A*, 530, A16
- Dai, Y., Ding, M. D., Chen, P. F., & Zhang, J. 2012, *ApJ*, 759, 55
- Dauphin, C., Vilmer, N., & Krucker, S. 2006, *A&A*, 455, 339
- Démoulin, P., Vourlidas, A., Pick, M., & Bouteille, A. 2012, *ApJ*, 750, 147
- Dudík, J., Janvier, M., Aulanier, G., et al. 2014, *ApJ*, 784, 144
- Feng, S. W., Chen, Y., Kong, X. L., et al. 2012, *ApJ*, 753, 21
- Forbes, T. G. 2010, in Heliophysics II. Plasma Physics of the Local Cosmos, ed. C. J. Schrijver, & G. L. Siscoe (Cambridge: Cambridge Univ. Press), 159
- Forbes, T. G., Linker, J. A., Chen, J., et al. 2006, *SSRv*, 123, 251
- Gopalswamy, N., Yashiro, S., Kaiser, M. L., Howard, R. A., & Bougeret, J.-L. 2001, *ApJL*, 548, L91
- Gui, B., Shen, C., Wang, Y., et al. 2011, *SoPh*, 271, 111
- Huang, J., Démoulin, P., Pick, M., et al. 2011, *ApJ*, 729, 107
- Janvier, M., Aulanier, G., Bommier, V., et al. 2014, *ApJ*, 788, 60
- Janvier, M., Aulanier, G., & Démoulin, P. 2015, *SoPh*, 290, 3425
- Janvier, M., Aulanier, G., Pariat, E., & Démoulin, P. 2013, *A&A*, 555, A77
- Kaiser, M. L., Kucera, T. A., Davila, J. M., et al. 2008, *SSRv*, 136, 5
- Karlický, M., & Bártá, M. 2011, *ApJ*, 733, 107
- Kerdraon, A., & Delouis, J.-M. 1997, in Proc. CESRA Workshop, Coronal Physics from Radio and Space Observations, ed. G. Trottet (Berlin: Springer), 192
- Kienreich, I. W., Muhr, N., Veronig, A. M., et al. 2013, *SoPh*, 286, 201
- Kliem, B., Karlický, M., & Benz, A. O. 2000, *A&A*, 360, 715
- Knock, S. A., & Cairns, I. H. 2005, *JGR*, 110, A01101
- Knock, S. A., Cairns, I. H., Robinson, P. A., & Kuncic, Z. 2003, *JGR*, 108, 1126
- Kong, X. L., Chen, Y., Li, G., et al. 2012, *ApJ*, 750, 158
- Lecacheux, A. 2000, in AGU Chapman Conference, Geophysical Monograph Series Vol. 119, Radio Astronomy at Long Wavelengths, ed. R. G. Stone, K. W. Weiler, M. L. Goldstein, & J.-L. Bougeret (Washington, DC: AGU), 321
- Lecacheux, A., Meyer-Vernet, N., & Daigne, G. 1981, *A&A*, 94, L9
- Lemen, J. R., Title, A. M., Akin, D. J., et al. 2012, *SoPh*, 275, 17
- Lin, J., & Forbes, T. G. 2000, *JGR*, 105, 2375
- Lin, J., Ko, Y. K., Sui, L., et al. 2005, *ApJ*, 622, 1251
- Lin, J., Raymond, J. C., & van Ballegooijen, A. A. 2004, *ApJ*, 602, 422
- Liu, R., Lee, J., Wang, T., et al. 2010, *ApJL*, 723, L28
- Liu, Y. D., Yang, Z., Wang, R., et al. 2014, *ApJL*, 793, L41
- Lugaz, N., Downs, C., Shibata, K., et al. 2011, *ApJ*, 738, 127
- Magdalenić, J., Marqué, C., Zhukov, A. N., Vršnak, B., & Žic, T. 2010, *ApJ*, 718, 266
- Mäkelä, P., Gopalswamy, N., Xie, H., et al. 2013, *SoPh*, 284, 59
- Mann, G., Aurass, H., Klassen, A., Estel, C., & Thompson, B. J. 1999, in 8th SOHO Workshop, ESA Special Publications Symp. 447, Plasma Dynamics and Diagnostics in the Solar Transition Region and Corona, ed. J.-C. Vial, & B. Kaldeich-Schümann (Noordwijk: ESA), 477
- Martínez Oliveros, J. C., Raftery, C. L., Bain, H. M., et al. 2012, *ApJ*, 748, 66
- Meyer-Vernet, N., Daigne, G., & Lecacheux, A. 1981, *A&A*, 96, 296
- Möstl, C., Rollett, T., Frahm, R. A., et al. 2015, *NatCo*, 6, 7135
- Nindos, A., Alissandrakis, C. E., Hillaris, A., & Preka-Papadema, P. 2011, *A&A*, 531, A31
- Panasenco, O., Martin, S., Joshi, A. D., & Srivastava, N. 2011, *JASTP*, 73, 1129
- Patsourakos, S., & Vourlidas, A. 2012, *SoPh*, 281, 187
- Patsourakos, S., Vourlidas, A., & Stenborg, G. 2010, *ApJL*, 724, L188
- Pick, M., Démoulin, P., Krucker, S., Malandraki, O., & Maia, D. 2005, *ApJ*, 625, 1019
- Ramesh, R., Lakshmi, M. A., Kathiravan, C., Gopalswamy, N., & Umaphathy, S. 2012, *ApJ*, 752, 107
- Reiner, M. J., Vourlidas, A., Cyr, O. C. S., et al. 2003, *ApJ*, 590, 533
- Robbrecht, E., Patsourakos, S., & Vourlidas, A. 2009, *ApJ*, 701, 283
- Saito, K., Poland, A. I., & Munro, R. H. 1977, *SoPh*, 55, 121
- Schmidt, J. M., & Cairns, I. H. 2012, *JGR*, 117, A04106
- Schou, J., Scherrer, P. H., Bush, R. I., et al. 2012, *SoPh*, 275, 229
- Shen, C., Wang, Y., Gui, B., Ye, P., & Wang, S. 2011, *SoPh*, 269, 389
- Smerd, S. F., Sheridan, K. V., & Stewart, R. T. 1974, in Proc. IAU Symp. 57, Coronal Disturbances, ed. G. A. Newkirk (Dordrecht: Reidel), 389
- Stenborg, G., Vourlidas, A., & Howard, R. 2008, *ApJ*, 674, 1201
- Sterling, A. C., Harra, L. K., & Moore, R. L. 2007, *ApJ*, 669, 1359
- Sterling, A. C., & Moore, R. L. 2004, *ApJ*, 613, 1221
- Vourlidas, A., Lynch, B. J., Howard, R. A., & Li, Y. 2012, *SoPh*, 284, 179
- Vršnak, B., Magdalenić, J., Aurass, H., & Mann, G. 2002, *A&A*, 396, 673
- Vršnak, B., Poletto, G., Vujić, E., et al. 2009, *A&A*, 499, 905
- Wang, Y.-M., & Sheeley, N. R., Jr. 1992, *ApJ*, 392, 310
- Wild, J. P., Sheridan, K. V., & Neylan, A. A. 1959, *AuJPh*, 12, 369
- Wuelser, J.-P., Lemen, J. R., Tarbell, T. D., et al. 2004, Proc. SPIE, 5171, 111
- Zhukov, A. N. 2011, *JASTP*, 73, 1096
- Zimovets, I., Vilmer, N., Chian, A. C.-L., Sharykin, I., & Struminsky, A. 2012, *A&A*, 547, A6
- Zucca, P., Carley, E. P., Bloomfield, D. S., & Gallagher, P. T. 2014a, *A&A*, 564, A47
- Zucca, P., Pick, M., Démoulin, P., et al. 2014b, *ApJ*, 795, 68
- Zuccarello, F. P., Bemporad, A., Jacobs, C., et al. 2012, *ApJ*, 744, 66